

Contents

1 Results	1
1.1 Basic equations, Laplace, Poisson, Diffusion etc.	1
1.2 Linear Mechanics	1
1.3 Nonlinear mechanics, tendon material	1
1.4 FEBio adapter, validation	1
1.5 Application: Subcellular Models	2
1.6 Application: Only Fibers, Monodomain	2
1.7 Application: Motoneuron with fibers	3
1.8 Application: Rosenfalck, artifical muscle geometry	3
1.9 Application: Simulation of Monodomain Fibers with EMG	3
1.10 Fiber Based Electrophysiology	3
1.11 Application: Static bidomain	30
1.12 Application: Multidomain	30
1.13 Application: Linear mechanics with artifical electrophysiology	32
1.14 Application: Fibers and Muscle contraction, no-precice	32
1.15 Application: Fibers and Muscle contraction, with tendons precice	34
1.16 Application: Neuromuscular system with Spindles and Prestretch	34
1.17 Application: Neuromuscular system with More Sensor Organs	38

1 Results

1.1 Basic equations, Laplace, Poisson, Diffusion etc.

1.2 Linear Mechanics

1.3 Nonlinear mechanics, tendon material

1.4 FEBio adapter, validation

cook's beam

1.5 Application: Subcellular Models

1.6 Application: Only Fibers, Monodomain

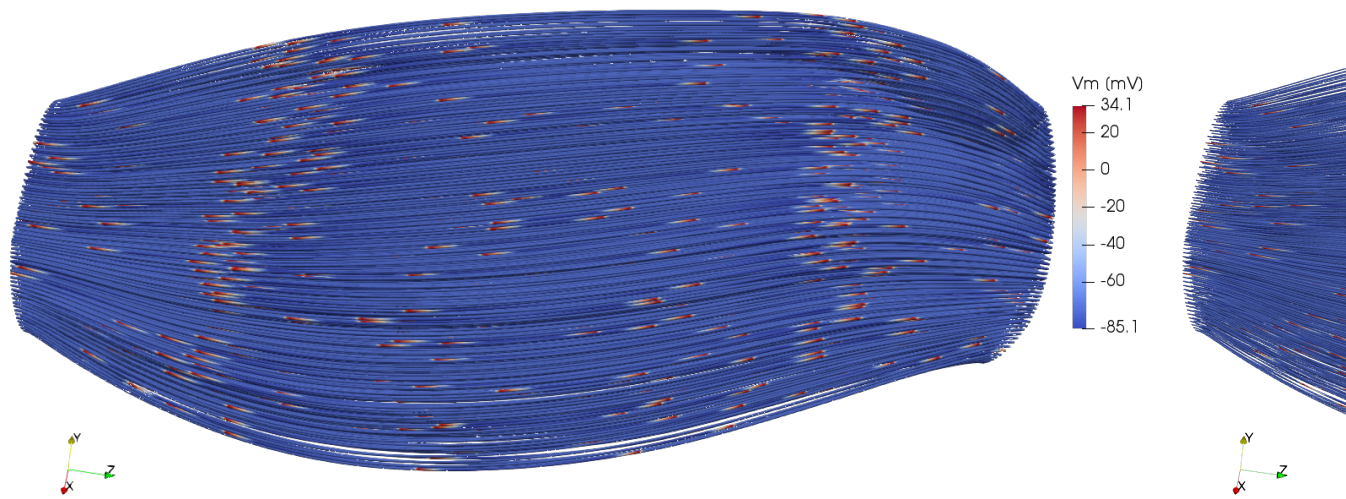


Figure 1.1: fibers mesh

1.7 Application: Motoneuron with fibers

1.8 Application: Rosenfalck, artifical muscle geometry

1.9 Application: Simulation of Monodomain Fibers with EMG

1.10 Fiber Based Electrophysiology

In this section, we consider surface EMG signals on the upper arm by simulating the activation of the biceps brachii muscle. [Section 1.10.1](#) introduces the considered domains and meshes and gives an overview of the simulation. Subsequently, we simulate various scenarios to investigate the effects of different model and numerical parameters on the resulting EMG signal. [Section 1.10.2](#) considers the effects of single motor units, [Sec. 1.10.3](#) considers the fat layer and [Sec. 1.10.4](#) shows effects of the mesh width. Then, [Sec. 1.10.5](#) presents a way to simulate realistic EMG electrodes and [Sec. 1.10.6](#) deals with the decomposition of EMG signals.

1.10.1 Overview of the EMG Simulation

[Figure 1.2](#) shows the setting of the biceps muscle and the tendons, which attach to the skeleton near the shoulder and to the ulna bone in the forearm. For the simulation of EMG, we only consider the muscle belly of the biceps muscle. The image [Fig. 1.2](#) shows muscle fibers inside the muscle, which run in longitudinal direction from the tendon at one end to the other tendon. The image also visualizes the results of an EMG simulation. The fibers are colored according to their transmembrane potential V_m and show some propagating action potentials.

The surface of the muscle is colored by the electric extracellular potential ϕ_e . In a reasonable approximation, the value of ϕ_e corresponds to the measured EMG signals on the skin surface. More realistic scenarios additionally consider volume conduction in a layer of adipose tissue on top of the muscle.

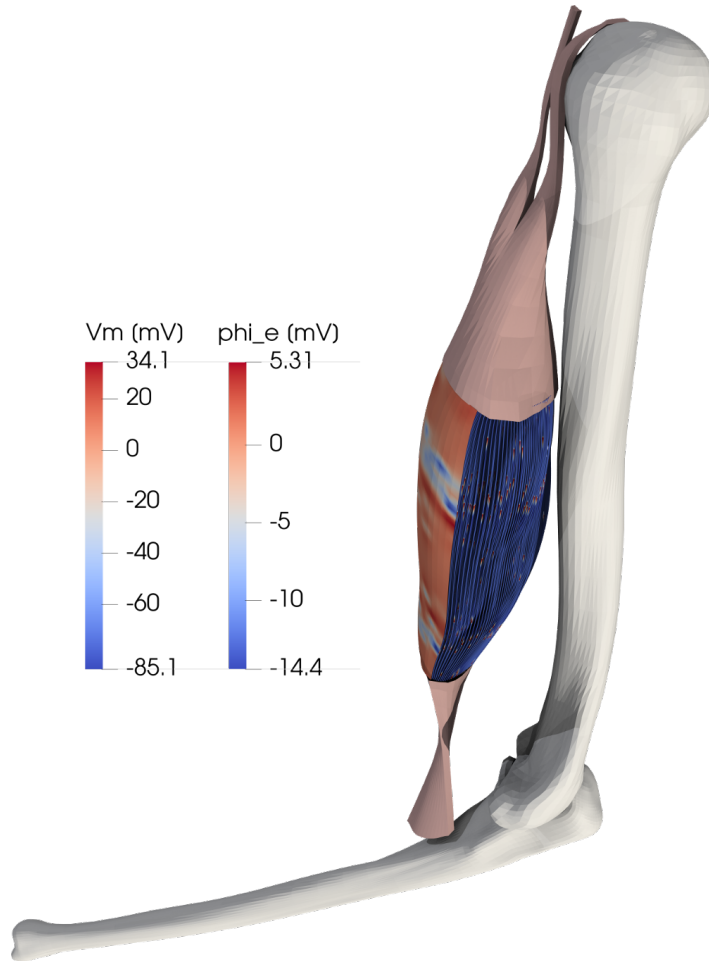


Figure 1.2: Considered setting for simulations of surface EMG on the upper arm, consisting of the biceps brachii muscle, tendons and bones. A simulation result of the membrane voltage V_m on the muscle fibers and the extracellular potential ϕ_e on the surface is shown.

For the EMG simulations, we solve the multi-scale model of fiber based electrophysiology. We solve the monodomain equation ?? independently on all 1D muscle fiber meshes. After fixed numbers of timesteps, we map the membrane voltage V_m from the 1D meshes to the 3D mesh. Subsequently, we solve the static bidomain equation ?? on the muscle domain and potentially the body fat domain to obtain the ϕ_e values on the skin surface.

[Figure 1.3](#) shows a close-up view of the active muscle fibers and the resulting EMG signals on the upper surface, which are identical to [Fig. 1.2](#). The scenario considers 1369 muscle fibers. It can be seen that they are approximately equally spaced as a result of the meshing algorithms described in ??.

The figure also shows the mesh of the muscle surface, which is colored according to the extracellular potential ϕ_e . It can be seen that the values correlate with the activation state

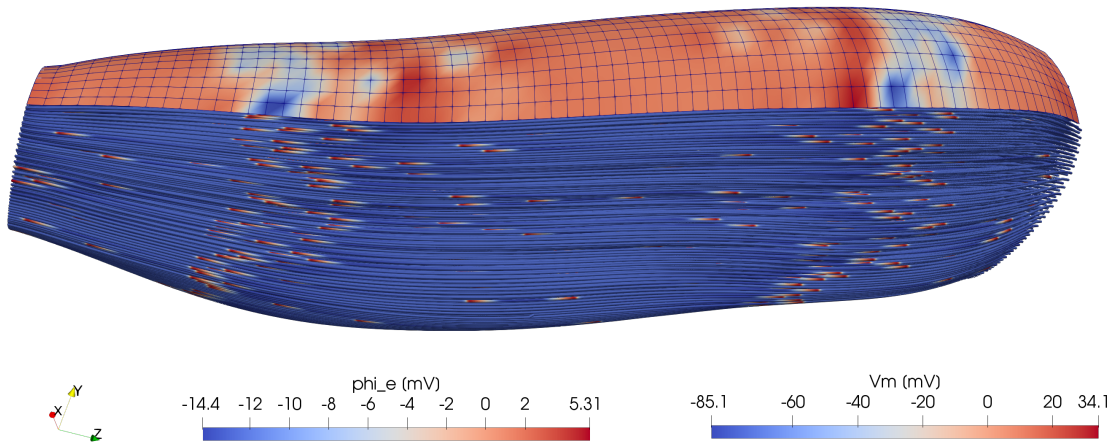


Figure 1.3: Overview of some of the meshes in an electrophysiology simulation: 1369 muscle fibers are located in the muscle belly. A 2D surface mesh on top of the muscle describes the computed EMG values. The visualized simulation is the same as in Fig. 1.2.

of the underlying fibers. At the two blue colored regions at the surface near the left and right ends of the muscle, the ϕ_e value is close to its minimum, while the majority of fibers exhibits its maximum positive V_m value. Towards the center of the muscle, the value of ϕ_e increases to its maximum, which reflects the hyperpolarization of the muscle fibers behind the propagating action potentials, i.e., the overshoot of the membrane voltage before it reapproaches the equilibrium level.

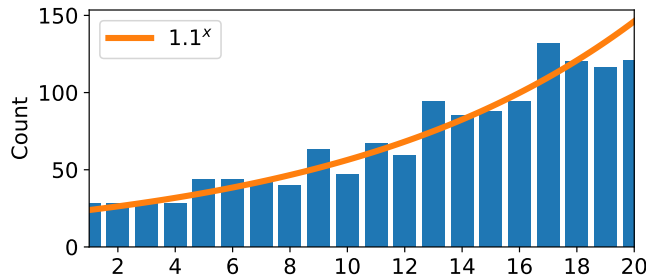
The lower left corner in Fig. 1.3 shows the coordinate frame that is used in all simulations. The z axis is approximately directed in fiber direction, the x and y axes are oriented in transverse direction and describe cross-sectional planes of the muscle.

1.10.2 Effects of Single Motor Units on the Electromyography Signal

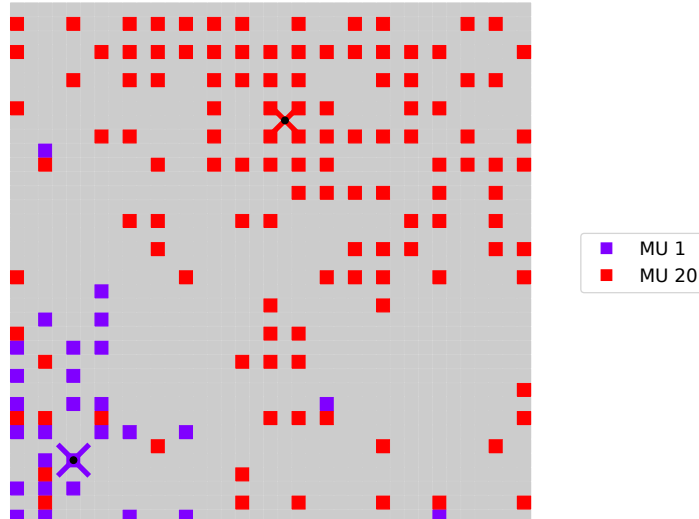
Next, we investigate how the surface EMG signals are influenced by several parameters of the simulation. We begin by studying EMG of only a single activated MU in the muscle.

The first scenario contains 20 MUs that have an exponentially progressing number of fibers as shown in Fig. 1.4a. The progression follows the function $y = c 1.1^x$ for an appropriate constant $c > 0$. The MU assignment is created using method 1a of the algorithm described in ??, where the MU territories are centered around given points and neighboring fibers are never part of the same MU.

Figure 1.4b shows the fibers that are assigned to the smallest and largest MUs, MUs 1 and 20. For this visualization, the muscle cross-section is mapped to the large gray square and every colored small square corresponds to one fiber. The purple and red crosses designate the center of MU territories for MU 1 and 20, respectively. In consequence, the fibers of MU 1 are mostly located at the bottom left of the cross-section and the fibers of MU 20 are mostly located in the upper right regions of the muscle cross-section. The visualization shows that the fibers of the same MU always have some spacing between them, which is due to the construction of the MU assignment algorithm.



(a) Exponential distribution of motor unit sizes. The diagram shows the motor unit numbers with the corresponding sizes or fibers counts of the MUs.



(b) Fibers that belong to motor units 1 and 20.

Figure 1.4: Assignment of the 1369 fibres to 20 motor units used in the simulation scenario for fiber based electrophysiology.

We begin with a simulation scenario where only a single MU is stimulated and study the effect on the surface EMG. The fibers of the respective MU are stimulated with a frequency $f = 24\text{ Hz}$ starting at time $t = 0\text{ ms}$. Each of the $13 \times 13 = 1369$ fibers consists of a mesh with 1481 nodes, the 3D mesh of the muscle contains $19 \times 19 \times 38 = 13\,718$ nodes and the 3D mesh of the fat layer contains $37 \times 5 \times 38 = 7030$ nodes. The domains are partitioned to 27 processes. The subcellular model of Hodgkin and Huxley is used, yielding a total number of more than $8.1 \cdot 10^6$ degrees of freedom. The timestep widths are $dt_{0\text{D}} = dt_{\text{splitting}} = 2.5 \cdot 10^{-3}\text{ ms}$, $dt_{1\text{D}} = 6.25 \cdot 10^{-4}\text{ ms}$ and $dt_{3\text{D}} = 5 \cdot 10^{-1}\text{ ms}$, leading to 4 subcycles for the 1D model in each splitting step and 200 splitting steps per solution of the bidomain equation.

We compute the linear systems for the initial potential flow problem to estimate fiber directions in the 3D domain and for the bidomain equation, which is solved in every timestep using a conjugate gradient solver. The program uses the `FastMonodomainSolver` class for the electrophysiology model. The Thomas algorithm solves the linear system of the diffusion problem. We use the "`vc`" optimization type and employ the scheme to only compute active fibers and the subcellular problems that are not in equilibrium.

The computation of a simulated time span with $t_{\text{end}} = 100\text{ ms}$ on a AMD EPYC 7742 64-core processor with 2492 MHz base frequency and 1.96 TB RAM takes approximately 100 s in the scenario that activates only the smallest MU and 126 s in the scenario that activates only the largest MU.

[Figure 1.5](#) shows the result for the scenario of activating the smallest MU, MU 1. In [Fig. 1.5a](#), the surface is shown in the background and colored according to the extracellular potential ϕ_e , which represents the EMG signal. The muscle volume is not shown, instead, the active parts of the respective fibers are displayed as tubes in the 3D domain. Their color visualizes the value of the transmembrane voltage V_m . In every of these small tube segments, the rising and declining shape of an action potential can be observed by the color progression from blue over orange to red for the rising part and back to blue for the declining part.

In this scenario, the fibers of MU 1 are stimulated three times within the first 100 ms at 0 ms, 41.6 ms and 83.3 ms. The innervation zone contains the starting points for the propagating stimulus on every fiber. The scenario positions the neuromuscular junctions randomly within the central 10% of every muscle fiber. The activated parts of the fibers visible in [Fig. 1.5a](#) correspond to the propagated action potentials of the last two stimulations in this scenario.

By comparing the results in Fig. 1.5a with the fiber distribution in Fig. 1.4b, it can be seen that fibers of MU 1 are located opposite of the muscle surface, which is at the upper side of the cross-sectional square diagram in Fig. 1.4b. The left side of the diagram in Fig. 1.4b corresponds to the lower part of the skin in Fig. 1.5a. This part of the skin is closer to the activated fibers and, thus, the effect on the surface EMG is highest for this region.

Figure 1.5b shows the skin surface as seen from the back in Fig. 1.5a. The active region is located at the right side in this image. It can be seen that the active region on the skin surface, which results from fibers of the activated MU 1, only spans a small portion of the surface.

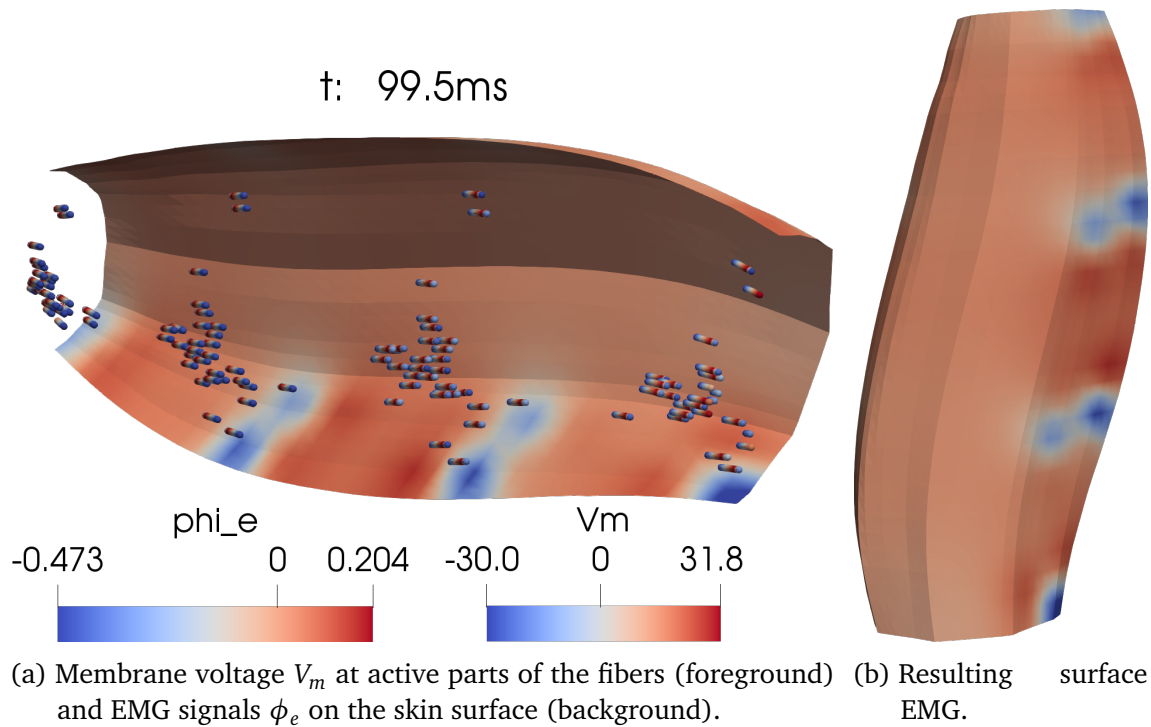


Figure 1.5: Simulation result at $t = 99.5$ ms where only motor unit 1 is activated.

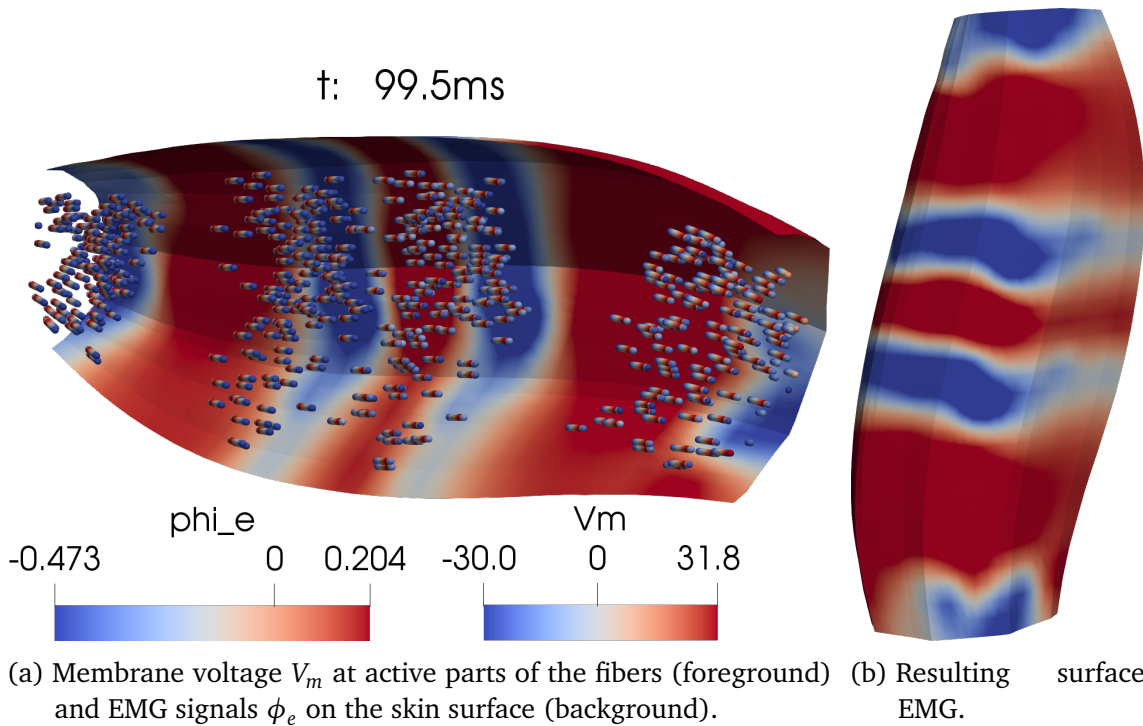


Figure 1.6: Simulation result at $t = 99.5$ ms where only motor unit 20 is activated, analogous to Fig. 1.5.

Figure 1.6 shows the analogous scenario that activates MU 20 instead of MU 1 is shown. Figure 1.6a shows that, now, more fibers are activated as MU 20 is larger than MU 1. According to the MU layout in Fig. 1.4b, the active fibers are also located closer to the skin surface. This layout results in a stronger EMG signal compared to the previous scenario.

The color coding in the two scenarios in Figures 1.5 and 1.6 is identical and it can be seen that the absolute value of the extracellular potential ϕ_e is larger in the scenario of MU 20. For the scenario with MU 1 in Fig. 1.5, the value range of the extracellular potential ϕ_e is $[-0.473 \text{ mV}, 0.204 \text{ mV}]$. For the scenario with MU 20 in Fig. 1.6, it is $[-0.834 \text{ mV}, 0.579 \text{ mV}]$, which is more than double the range.

Figure 1.6b shows the overall EMG signal on the skin surface for MU 20. Compared to the result of MU 1 in Fig. 1.5b, nearly the inverse region is activated. It can, thus, be observed that the EMG signal is highly influenced by the location and size of the MUs. MUs with territories closer to the skin surface have a larger effect on the EMG signals than MUs that are located further away. As seen in Fig. 1.5b, the influence of fibers completely vanishes for more than a certain distance. On the contrary, the effects of several close

fibers add up such that large MUs located near the surface have the most impact on the resulting EMG signal.

1.10.3 Effects of the Fat Layer on the Electromyography Signal

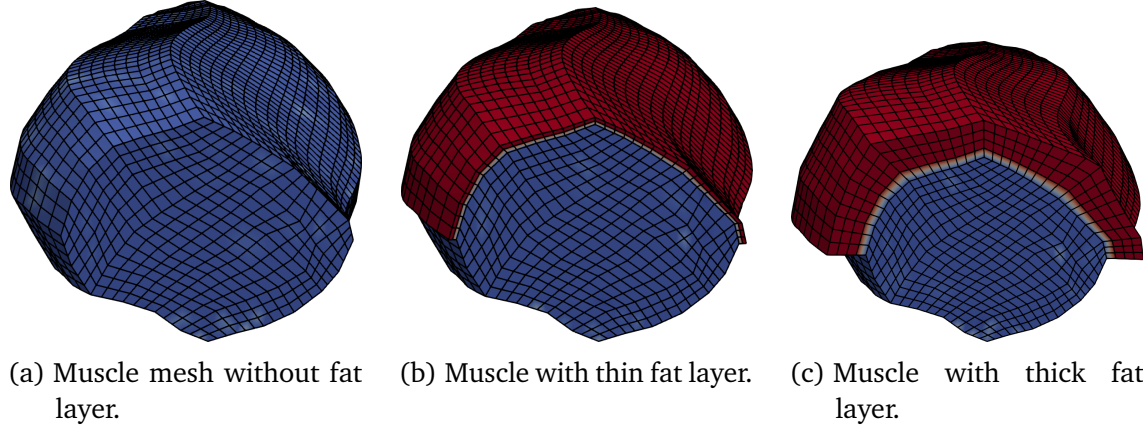


Figure 1.7: Meshes for the muscle domains (blue) and the layer of adipose tissue (red) used in the study to compare different fat layer widths.

In the next study, we investigate the effect of the fat layer on the resulting EMG signals. The same scenario as in the previous section is used, except that the size of the body fat domain is varied and the activated MUs are chosen differently. We consider the domains and meshes shown in Fig. 1.7: Scenario (a) only considers the muscle domain without additional fat layer. Scenario (b) adds a thin fat layer with thickness of 2 mm, discretized by two layers of finite elements. Scenario (c) considers a fat layer with thickness of 1 cm and four layers of elements. The scenario in the previous section also used this thick fat layer.

In this series of experiments, the first 10 MUs are activated with different stimulation frequencies ranging from 7 Hz for the smallest MU to 15.15 Hz for MU 10. The runtime of the simulation for one scenario on the same hardware as in the previous section is approximately 9 min.

Figure 1.8 shows the simulation results at $t = 100$ ms for the three scenarios with different fat layers. The figure uses the same color coding for the extracellular potential ϕ_e in all three scenarios. It can be seen that the volume conduction in the fat layer significantly smooths the resulting EMG signal, especially for the thick fat layer. The scenarios with no fat layer and the thin fat layer also exhibit a small difference. This

effect has implications for experimental studies, where the EMG recordings capture the less resolved spatial information, the more tissue is located between the muscle and the surface electrodes.

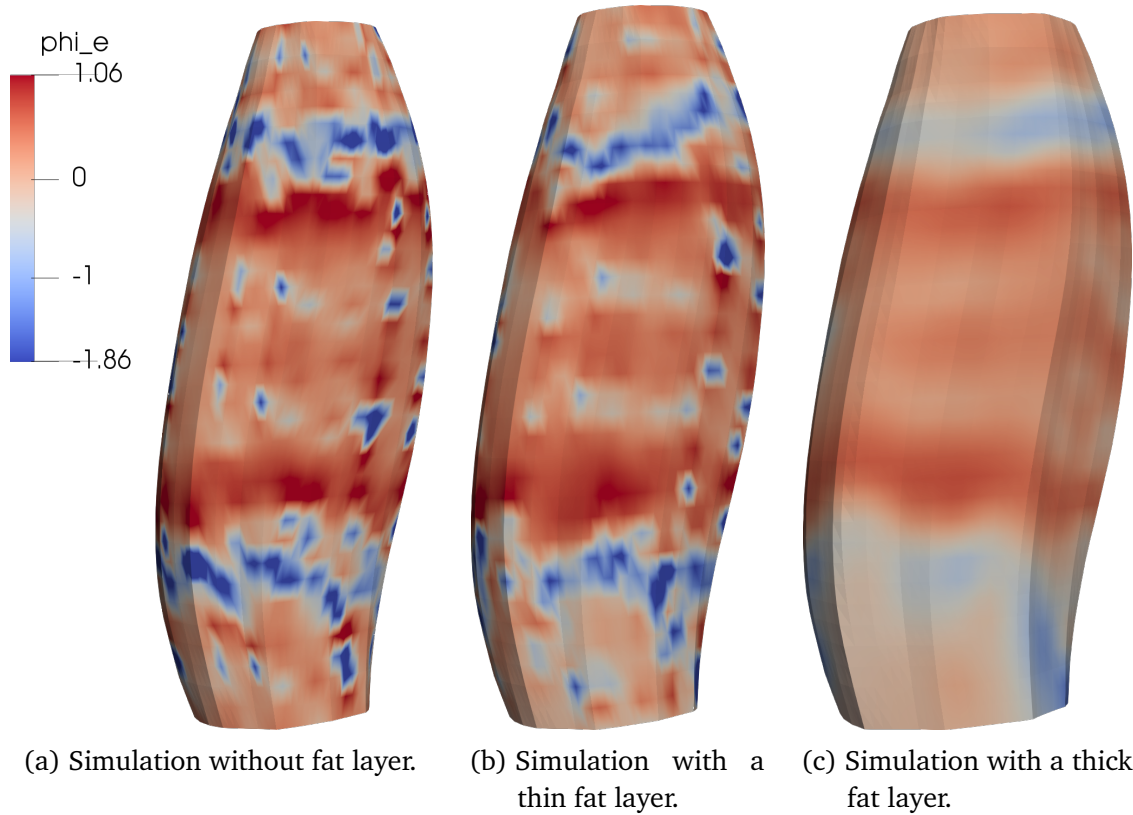


Figure 1.8: Simulated surface EMG signals for the different fat layers shown in Fig. 1.7.

How To Reproduce

The simulations in this section use the examples `examples/electrophysiology/fibers/fibers_emg` and `examples/electrophysiology/fibers/fibers_fat_emg` with the variables file `20mus_fat_comparison.py`.

The scenario data that is necessary to run the simulations are given in the repository at github.com/dihu-stuttgart/performance in the directory `opendihu/18_fibers_emg`. The main scripts that runs the simulations for the two sections are the following:

```
./run_single_MUs.sh  
./run_compare_fat_layer.sh
```

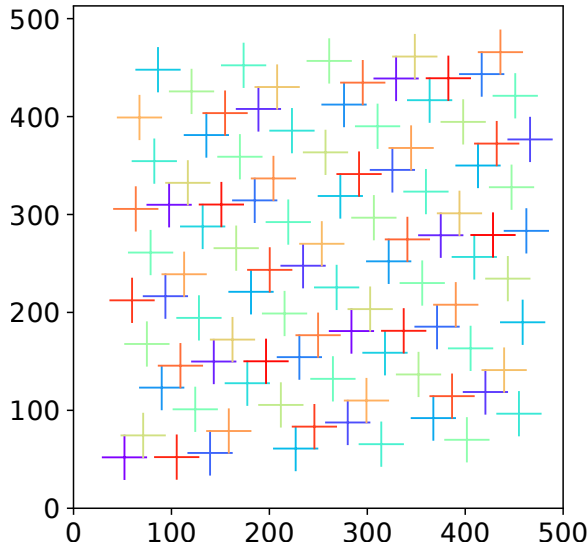


Figure 1.9: MU territory center points. The shown center points of the 100 motor units are used in all different scenarios within the study of different mesh widths.

1.10.4 Effects of the Mesh Width on the Electromyography Signal

Next, we compare the simulated EMG signal for different numbers of fibers and resolutions of the 3D mesh. We consider a scenario with 100 MUs and increase the spatial resolution and the number of processes that execute the computation on the supercomputer Hawk at the High Performance Computing Center Stuttgart.

We compute scenarios with between 1369 and 273 529 fibers. The specified number of 100 MUs have to be assigned to these numbers of fibers for each scenario. We use the method 1a of the algorithm described in ???. The MU territories are centered around quasi-randomly generated center points, as shown in Fig. 1.9. It can be seen that the MU territory center points are homogeneously distributed in space.

For every fiber, the algorithm assigns a MU with a close center point with higher probability than a MU whose center is located further away. The total number of fibers per MU is progressing exponentially for the MUs from 1 to 100. The progression is described by an exponential function with basis 1.02. Figure 1.10 shows the MU size distributions for four scenarios with increasing numbers of fibers from 169 to 273 529. For 169 fibers in Fig. 1.10a, not all 100 MUs get associated with a fiber. Further, it can be seen that the error of the actual size distribution to the exponential function decreases with increasing number of fibers. For the largest scenario in Fig. 1.10d, the MU sizes range from 602 to 6097 fibers.

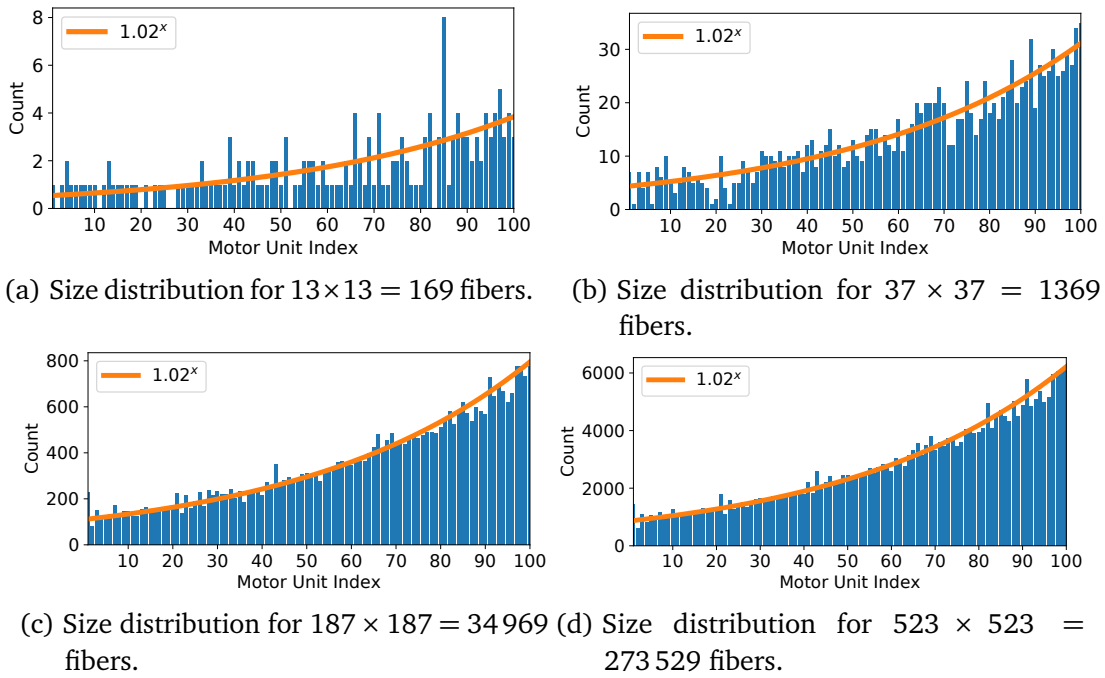


Figure 1.10: Distribution of the sizes of the 100 MUs in the scenarios with different number of fibers.

The number of approximately $3 \cdot 10^6$ fibers in the largest scenario matches the realistic number in a biceps muscle [Mac84]. The number of MUs can be higher in reality, e.g., by a factor of 5 [Fei55]; [Mac06]. Thus, the modeled MUs in this scenario can be seen as a combination of multiple real MUs. Especially the smallest MUs, which in reality can consist of only some dozens of fibers, are lumped by the first few MUs in our scenario. We restrict the number of MUs to 100 to be able to simulate the same problem also with smaller resolutions, e.g., with only 169 fibers.

As described in ??, the MU assignment algorithm asserts that neighboring fibers are part of different MUs by splitting the assignment problem for the given set of fibers into four smaller problems and then interleaving the results of the four parts. Figure 1.11a shows the first such part, where 25 MUs are associated to a subset of the fibers for the largest scenario with 273 529 fibers. It can be seen that the three visualized MUs are largely clustered around their MU territory centers.

The final association of fibers and MUs is given in Fig. 1.11b. Six selected MUs are shown of which the first, MU 1, corresponds to the first MU in Fig. 1.11a. The figure shows that the fibers, especially the ones of the larger MUs, are distributed far across the muscle. Comparing the smallest MU, MU 1, with the largest MU, MU 100, gives an impression of the MU size differences in this scenario.

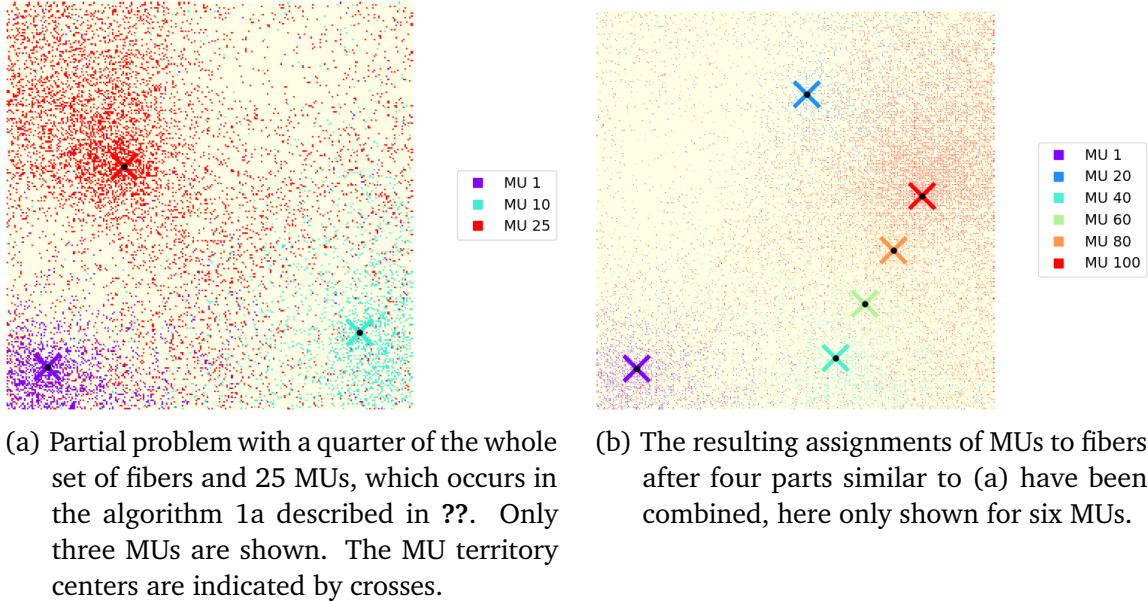


Figure 1.11: Association of MUs to the fibers. The square domain corresponds to a cross-section in the muscle, every colored point is one fiber and the color corresponds to the MU.

#fibers	3D stride		2D surface mesh	3D dofs (k=1000)	0D dofs	#proc.	#comp. nodes
	x	y					
$37^2 = 1369$	2	8	19×186	67k	8109k	144	3
$67^2 = 4489$	2	4	34×371	428k	26592k	448	7
$109^2 = 11881$	2	3	55×495	1497k	70383k	1152	18
$187^2 = 34969$	2	2	94×741	6547k	207156k	3600	57
$277^2 = 76729$	2	1	139×1481	28614k	454542k	7744	121
$523^2 = 273529$	2	1	262×1481	101661k	1620M	26912	421

Table 1.1: Parameters of spatial discretization and parallel partitioning for the EMG study. The 3D stride refers to the stride with which the 3D mesh is generated from the 0D points. The 2D surface is the output of the EMG and corresponds to one face of the 3D mesh.

The numeric parameters of the simulations are the same as in the last section. The scenario is computed for a simulation time span of 1 s. The MUs are activated in a ramp every 2 ms such that all MUs are active after 200 ms. The fiber radius and the stimulation frequency for the MUs are exponentially distributed with basis 1.02, similar to the MU size. The fiber radius increases from 40 μm to 55 μm and the stimulation frequency decreases from 24 Hz to 7 Hz for MUs 1 to 100. A random frequency jitter of 10 % is assumed.

The surface to volume ratio A_m of the membrane is determined by assuming a cylindrical shape and can be computed from the fiber radius r by $A_m = 2/r$ [Klo20]. We model 70 % slow twitch and 30 % fast twitch fibers. Accordingly, the membrane capacitance C_m is set to $C_m = 0.58 \frac{\mu\text{F}}{\text{cm}^2}$ for the 70 smallest MUs and to $C_m = 1 \frac{\mu\text{F}}{\text{cm}^2}$ for the 30 largest MUs.

[Table 1.1](#) lists the spatial discretization and parallel partitioning parameters. The first column shows the number of fibers. Their number increases, however, the mesh resolution of every 1D fiber mesh stays constant at 1480 elements per fiber. The stride that defines the 3D mesh is given in the second and third columns. The stride in radial direction of the muscle, i.e., in the x and y coordinate directions, stays constant. Because the fiber density increases, the 3D mesh is refined accordingly. The stride along the fibers, i.e., in z direction is reduced such that the mesh widths of the 3D mesh in all three coordinate directions remain balanced.

The resulting EMG recordings of each simulation are described by 2D meshes, which contain the values of the 3D muscle meshes without fat layer on the surface at one side of the muscle. The fourth column in [Tab. 1.1](#) lists the dimensions of these surface meshes.

The next two columns list the number of dofs in the 3D mesh and the number of dofs in all fibers. For these scenarios, it is not practical to output the 3D mesh or the 1D fiber meshes in regular time intervals, because this would produce large amounts of data that could hardly be processed. Instead, we only output the 2D surface mesh in the ParaView format every 10 ms.

The last two columns in [Tab. 1.1](#) show the numbers of processes and compute nodes that are used on Hawk. One compute nodes contains 128 physical cores and always four cores share a 16 MiB level three (L3) cache. However, we decide to use only 64 cores per compute node, i.e., two cores per L3 cache, because measurements showed that this reduces the overall computation times more than is lost by the decreased parallelism of not using all physical cores on a compute node. For example, the total computation time of this scenario with a timespan of 1 s is 2 h20 min for the scenario with 76 729 fibers and 7744 processes.

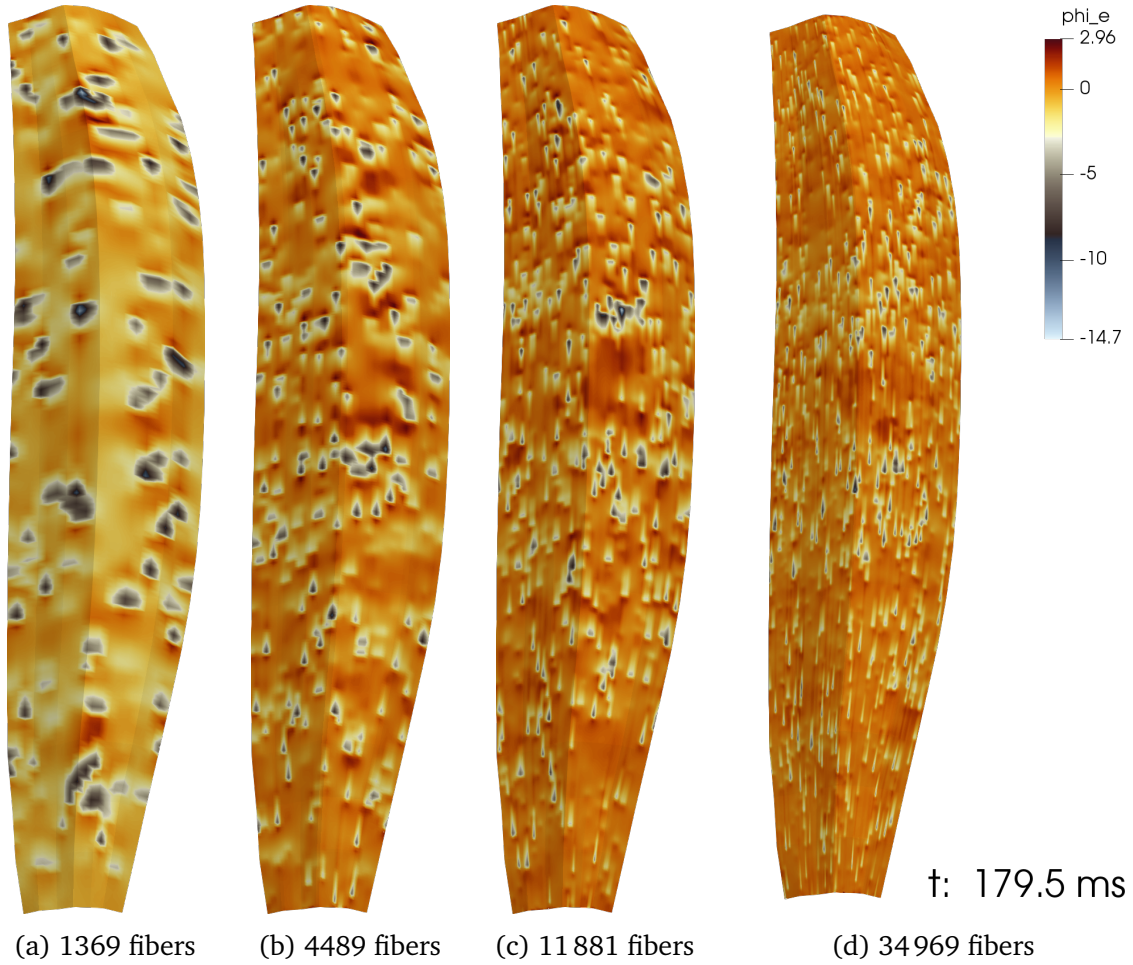


Figure 1.12: Simulated surface EMG signals for different numbers of fibers and different mesh widths of the 3D mesh.

[Figures 1.12](#) and [1.13](#) show the resulting surface EMG signals for different resolutions. The color visualizes the value of the extracellular potential ϕ_e according to the shown color bar. Because of sign conventions in the definitions of the electric potentials, the spikes in the EMG signals, which result from the action potentials, are negative.

The resulting electric potentials in [Fig. 1.12](#) exhibit different regions of higher activation that move over time from the center of the muscle towards its ends. The size of these regions at time $t = 179.5$ ms decreases from [Fig. 1.12a](#) to [Fig. 1.12d](#) as the mesh width decreases. Dark colored strong signals can be seen, which mainly correspond to fibers that are located directly underneath the shown muscle surface. Apart from these strong signals, also weaker artifacts occur, which are shown in yellow and orange colors. They result from the superposition of several fibers of the same or different MUs. The number of recognizable weak signals is higher for the simulations with higher numbers of fibers and finer mesh resolution.

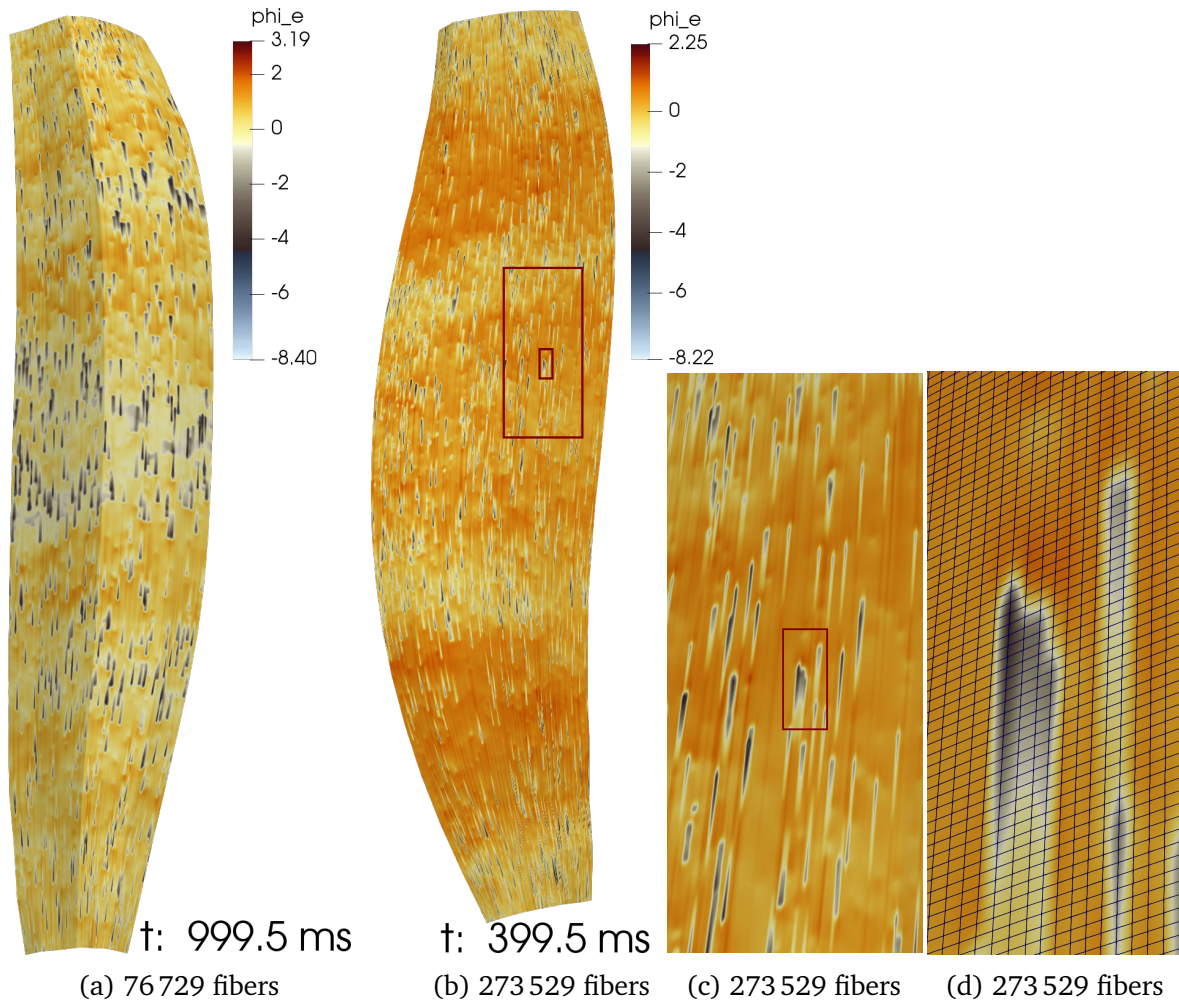


Figure 1.13: Simulated surface EMG signals for different numbers of fibers and different mesh widths of the 3D mesh, continued from Fig. 1.12

How To Reproduce

Use the following commands to run the EMG simulation of the biceps muscle with fat layer and electrodes:

```
cd $OPENDIHU_HOME/examples/electrophysiology/fibers/fibers_fat_emg/
→ build_release
mpirun -n 16 fibers_fat_emg ../settings_fibers_fat_emg.py 50mus.py
cd out/50mus
plot_emg.py ./electrodes.csv ./stimulation.log 25900 26000 # plot
→ the result, here for time span 25.9s - 26s
```

1.10.5 Simulation of EMG electrodes

While the surface EMG simulation results as presented in the last section in Fig. 1.12 are suited for insights into the temporal and spatial variation of the electric potential, real experiments are constraint to capture values at the discrete locations of electrodes. For some applications such as the evaluation of EMG decomposition algorithms, it is beneficial to obtain simulated values at electrode locations.

One possibility would be to extract nodal values from the simulated surface meshes to simulate electrodes. However, the distance between the nodes in the mesh is not constant in the whole mesh, whereas EMG electrode arrays have fixed inter electrode spacings. We, therefore, follow a different approach and allow to directly specify a grid of electrodes close to the muscle surface. These points are then mapped onto the surface of the muscle and the respective values are calculated by evaluating the finite element interpolant at the respective locations.

In OpenDiHu, a 2D grid of surface electrodes can be defined in the Python settings file by specifying the grid parameters and inter electrode distances. In result, the simulation distributes the electrodes to the processes according to the parallel partitioning of the 3D mesh, evaluates the computed EMG values at the respective locations and outputs them in a single text file of comma separated values.

Figure 1.14 shows simulation results of the fiber based electrophysiology model with 49 fibers, fat layer and an array of 12×32 electrodes. The electrodes are visualized as spheres. The muscle fibers below the fat layer are colored according to the transmembrane voltage V_m . Of the fat layer only the upper surface is shown and colored according to the extracellular potential ϕ_e . The EMG electrodes capture the values of the scalar field ϕ_e at their locations. The color coding for the electrodes has a different EMG color scale to make the resulting signals more distinguishable. Two activated bands across the muscle surface can be seen, which are also present in the electrode values.

To visually evaluate the simulated EMG signals at the electrodes, OpenDiHu provides utilities to create the visualizations shown in Fig. 1.15. Figure 1.15a shows a still image from an animation. On the upper right, the grid of electrodes is displayed. The EMG signal at the electrodes is given by the colored tiles and changes over time. At the bottom of the image, the activation times of the MUs are visualized. Every horizontal line corresponds to one MU. The colored markers indicate when the respective MU fires. As the shown example visualizes data for 40 s, the individual firing times are not distinguishable. In the animation, a vertical bar moves over the time axis and indicates the current simulation

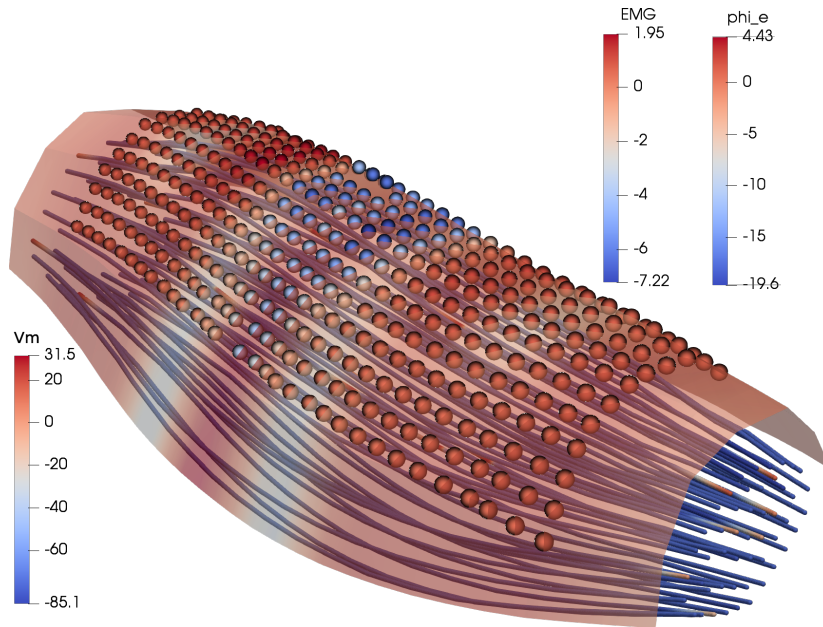


Figure 1.14: Simulation of surface EMG and capturing electrodes. The scenario contains 49 muscle fibers, a fat layer of which only the surface is shown and a grid of 12×32 equidistant electrodes.

time. The picture displays the EMG values at time $t = 25.975$ s. The upper left of the image shows a text with static information about the dataset, containing the electrode grid size, the inter electrode distance (IED), the end time, the sampling frequency of the electrodes, i.e., the frequency with which the computed EMG signals values are stored to the output file, and the number of MUs.

[Figure 1.15b](#) shows another, static visualization of simulated EMG data. The diagram contains boxes for all electrodes in the 12×32 grid. The value of the EMG signal is plotted over time in every box for the respective electrode. [Figure 1.15b](#) visualizes the data of [Fig. 1.15a](#) for the time interval [25.9 s, 26 s]. The diagram enables experts to visually identify propagating action potentials from the tile columns. The propagation velocity of the action potentials can be estimated from the time shift of matching spikes in vertically adjacent boxes.

1.10.6 Decomposition of Surface EMG Signals

Surface EMG recordings are a valuable tool to gain insights into the neuromuscular system. They are used, e.g., for the diagnosis of muscular disorders and in clinical studies that aim to advance biomedical understanding.

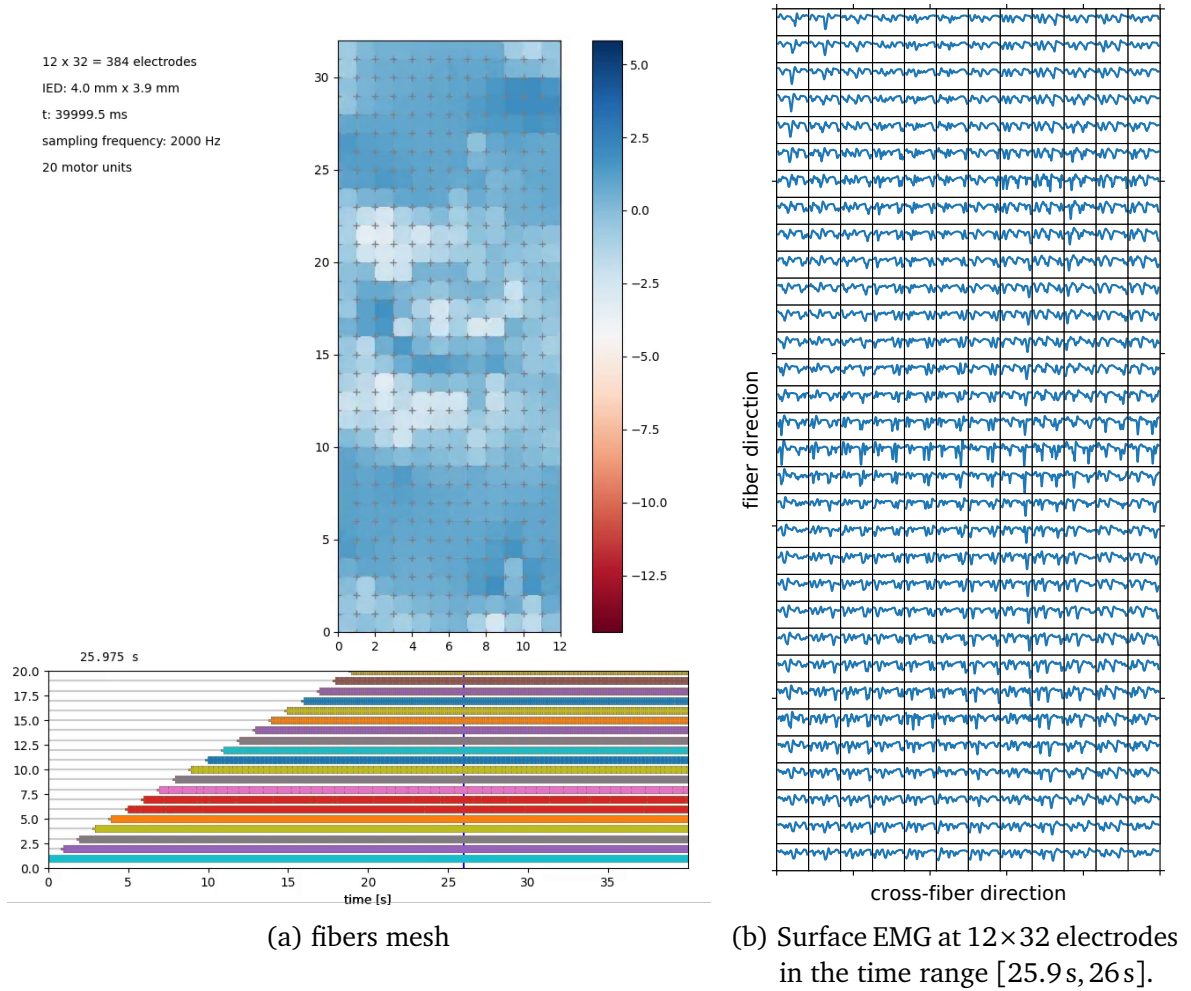


Figure 1.15: Simulation of surface EMG using electrodes.

As described earlier, the EMG signals on the skin surface originate from the activated muscle fibers. Effects from volume conduction of action potentials on all muscle fibers are superpositioned and contribute to the EMG signal. The scaling of the contributions to the overall signal depends on several factors, such as the distance of the fibers to the skin surface. As all fibers in the same MU get activated simultaneously, each MU's contribution shows a characteristic “shape” in the resulting surface EMG signal. This shape is influenced by the number and location of the muscle fibers relative to the electrodes and the location of the neuromuscular junctions.

In our simulation, the location of the neuromuscular junctions is chosen pseudo-randomly (but deterministic) during initialization in the central 10 % of every muscle fiber. [Figure 1.16](#) shows the state of a simulation with 1369 fibers at $t = 1$ ms, where all fibers have been activated at $t = 0$ ms. The color coding indicates the potential V_m of the membrane, which at the shown time has only depolarized near the locations of the neuromuscular

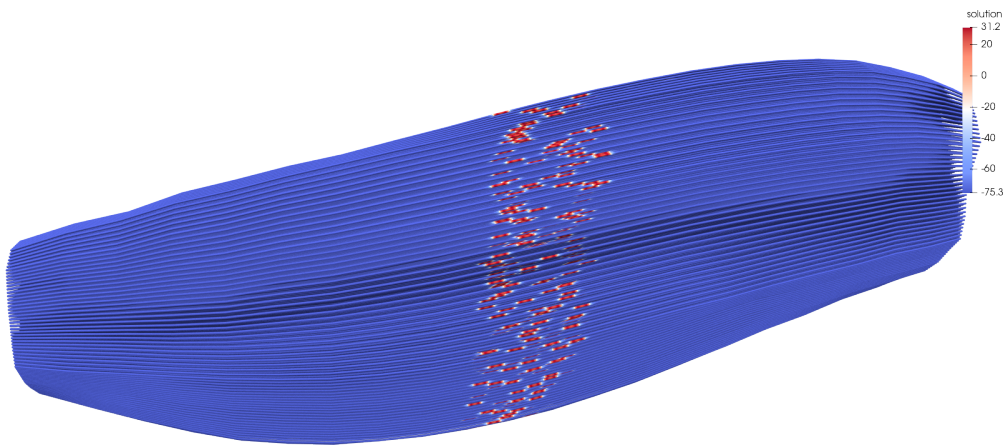


Figure 1.16: A simulation result that reveals the locations of the neuromuscular junctions.

The figure depicts 1369 fibers after 1 ms that have initially been stimulated at the neuromuscular junction. The color coding corresponds to the membrane potential V_m , which has a positive value near the points of stimulation.

junctions.

Methods exist that seek to decompose the surface EMG signal into the contributions of the individual MUs. One popular method is *Gradient Convolution Kernel Compensation* (gCKC) [Hol07a]; [Hol07b], which, in the following, will be outlined and then applied on simulated data.

Most decomposition methods, including the gCKC algorithm, assume that the EMG signal at an electrode is composed of the convolutional mixture of N filters of the MU activity. The activity of each MU $k \in \{1, \dots, N\}$ is described by the innervation pulse trains that activate the fibers of MU k , given as a point process of neural inputs at stimulation times φ_r . The source signal s_k in the muscle that represents the effect of MU k is described as a filter over these neural drives, $s_k(t) = \sum_r \delta(t - \varphi_r)$, where δ is the dirac delta function.

The vector of observed EMG values $\mathbf{x} \in \mathbb{R}^m$ at a time t is composed of the temporal convolution over L time-shifted sources \mathbf{s} and a term $\boldsymbol{\omega}$ of additive Gaussian noise:

$$\mathbf{x}(t) = \sum_{\ell=0}^{L-1} \mathbf{H}(\ell) \mathbf{s}(t - \ell) + \boldsymbol{\omega}(t).$$

Here, \mathbf{H} is the $m \times n$ mixing matrix for m observations and n MU sources and $\mathbf{s} = (s_k)_{1, \dots, n}$ is the vector of source signals. The sum over L previous values in this convulsive mixture can be reformulated by moving the summation into the matrix-vector product. The dimensions of the matrix \mathbf{H} and the vector \mathbf{s} are extended accordingly. Inversion of the

extended mixture matrix yields the separation vectors, with which the innervation pulse trains φ_r of the MUs can be recovered from the recorded EMG signals \mathbf{x} . The gCKC algorithm performs the inversion indirectly by solving a derived optimization problem using a gradient descent scheme.

The gCKC decomposition algorithm is implemented in the DEMUSE software, a commercial, MATLAB based tool that allows automatic and semi-automatic EMG decomposition [Hol08]. In collaboration with Lena Lehmann from the *Institute of Signal Processing and System Theory* and the *Institute for Modelling and Simulation of Biomechanical Systems*, we evaluated the performance of gCKC decomposition on simulated surface EMG signals.

We simulate fiber-based electrophysiology scenarios with fat layer and 1369 fibers using the same model parameter as in Sec. 1.10.4. In the first scenario, a fat layer with thickness of 1 cm is modelled. The simulated EMG signal is sampled in an electrode array with a frequency of 2 kHz and a grid size of 12×32 fibers, as shown in Fig. 1.15.

Figure 1.17 shows the firing times of the 20 MUs in the first 10 s. The different MUs are initially activated every 100 ms to generate the shown “ramp” activation pattern, which later helps to identify the recovered MUs from the decomposition. From $t = 1.8$ s on, all MUs fire with their respective constant frequency, subject to jitter values of 10 %.

In this first scenario, the gCKC decomposition algorithm was applied on the first $t = 40$ s of simulated EMG data. The preconfigured algorithm in DEMUSE was used without manual intervention. While the simulated EMG recording consisted of an electrode grid of 12×32 fibers, only a rectangular subset of 5×13 channels at the lower center of the grid was used for the decomposition to mimic a realistic electrode array size. The DEMUSE software discarded four of these 65 channels as being invalid.

Figure 1.17 shows the innervation pulses that were detected by DEMUSE as red vertical markers. A time span of 50 s was simulated of which only the first 11 s are visualized in Fig. 1.17. DEMUSE found four MUs in this scenario, i.e., 20 % of the 20 simulated MUs. The recovered MUs were identified in the set of simulated MUs by matching the average firing frequency and the activation onset time in the ramp scheme. A first visual comparison with the original stimulation times given by the black markers shows a good agreement.

In this scenario, the association of fibers with MUs followed an exponential MU size progression with a basis of approximately 1.2, as shown in Fig. 1.18a. The smallest MU contained two fibers and the largest MU had 256 fibers. The method 1 described in ?? was used to generate the association between fibers and MUs.

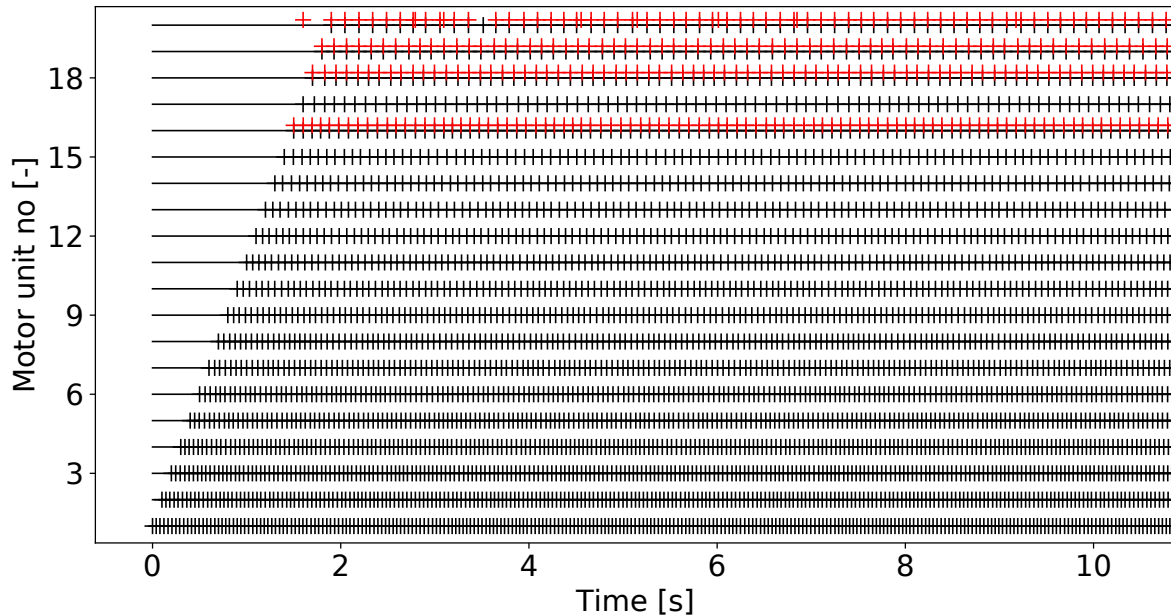


Figure 1.17: Match of EMG decomposition results with simulated data. The firing pattern over time for the 20 MUs in the simulation is shown by black markers. The recovered firing times of the gradient convolution kernel compensation algorithm are given by the red markers. The algorithm detected the four MUs 16, 18, 19 and 20.

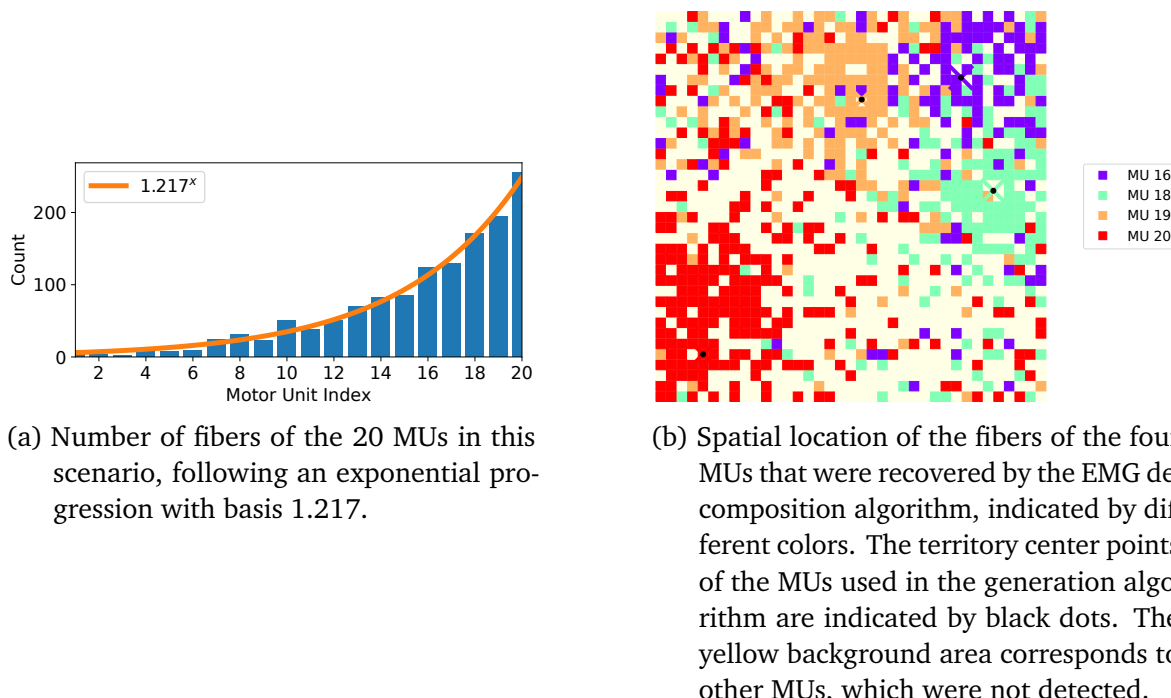


Figure 1.18: Association of the fibers with motor units for the first scenario with 20 MUs, given in Fig. 1.17.

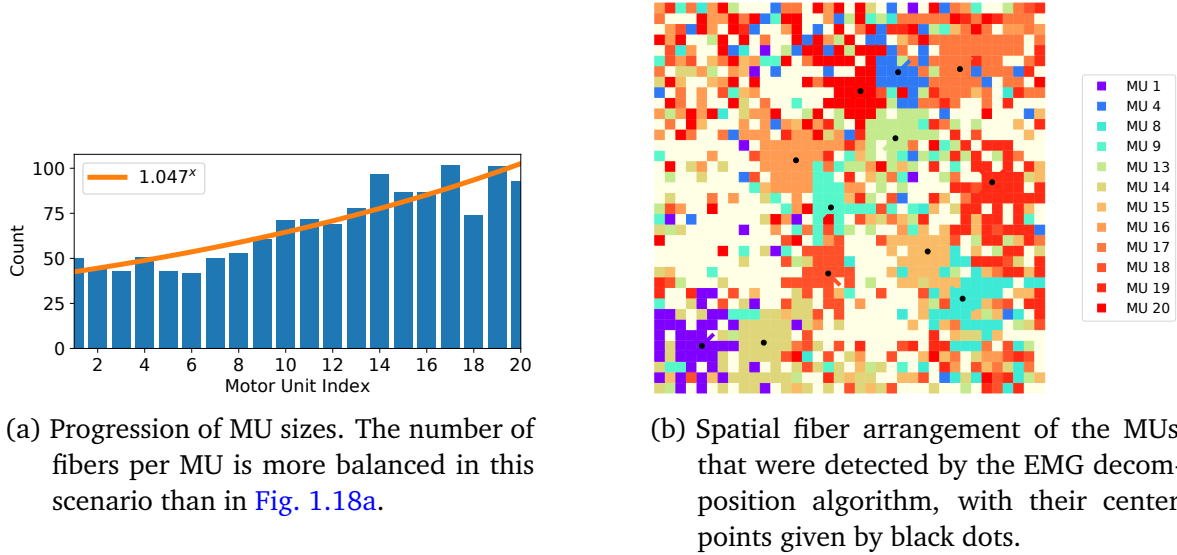


Figure 1.19: Association of the fibers with motor units for the second scenario with 20 MUs, given in Fig. 1.20.

Figure 1.18b depicts the location of the four MUs that were detected by DEMUSE. The detected MUs have the indices 16, 18, 19 and 20 and correspond to four of the five largest MUs. It can be seen that MUs 18 to 20 are located mainly in the upper half of the muscle cross-section, in proximity to the electrode array at the top of the diagram. The MU with the most fibers, MU 20, was detected by the decomposition algorithm even though it is located at the lower left of diagram at a large distance to the skin surface.

Two further scenario were simulated with the same parameters as the first scenario in Fig. 1.17, but instead with 50 and 100 MUs. In these datasets, DEMUSE was able to detect 8 and 12 MUs, which corresponds to 16 % and 12 %.

Moreover, another scenario with 20 MUs was computed, but the fat layer was varied to have a thickness of only 2 mm instead of 1 cm. In addition, the association scheme between MUs and fibers was changed to the one shown in Fig. 1.19. The exponential distribution of MU sizes only varied between 42 and 102 fibers per MU, corresponding to a basis in the exponential function of approximately 1.05 instead of 1.2.

Figure 1.20 shows the results of the EMG decomposition with the gCKC algorithm for this second scenario with 20 MUs. DEMUSE successfully decomposed the signal into 13 MUs, corresponding to 65 % of the 20 simulated MUs. DEMUSE also determined two additional MUs, which we do not consider part of the set of successfully recovered MUs. The first dataset only consists of ten innervation pulses, and the second pulse train contains high frequency oscillations. In this scenario, the software marked only one

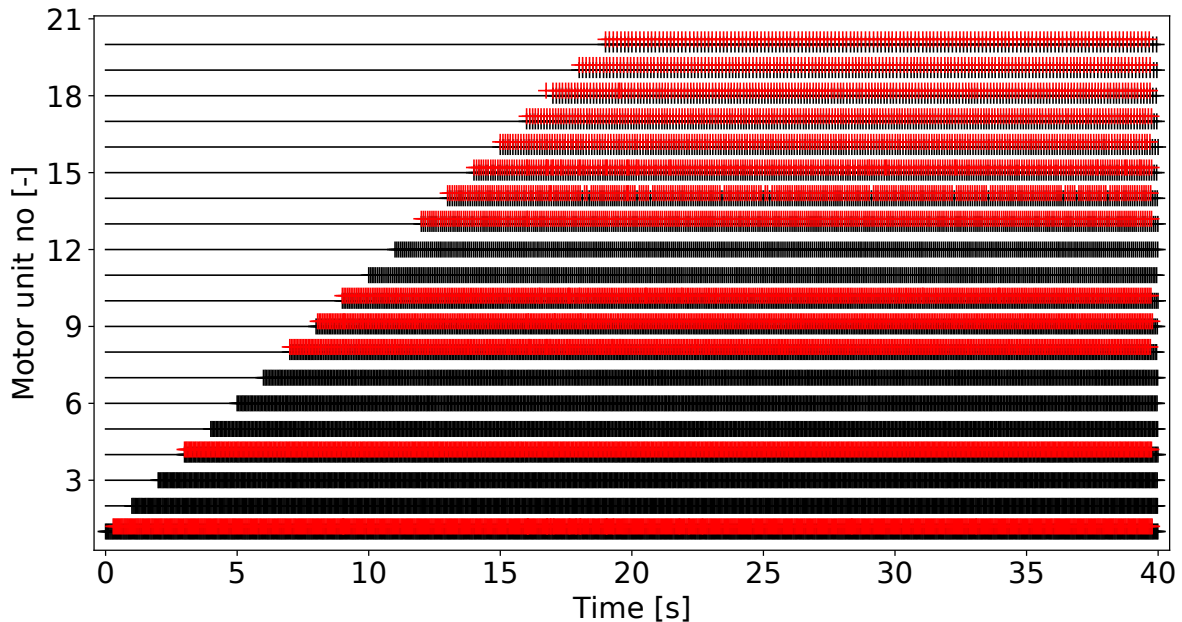


Figure 1.20: Activation pattern for the second scenario with 20 MUs. The activation times used in the simulation are shown as black markers, the recovered activation pulses of the EMG decomposition algorithm are shown as red markers.

EMG recording channel as invalid, which means that more data was considered by the decomposition algorithm than in the first scenario with 20 MUs.

Similar to the previously presented scenario, the larger MUs were detected with a higher probability than the smaller MUs. In this scenario, the eight largest MUs were successfully found. [Figure 1.19b](#) shows the spatial arrangement of the detected MUs. The area of the muscle cross section that is occupied by undetected MUs is again distributed more distantly to the skin surface at the upper boundary. However, the recovered MUs 1 and 14 are nevertheless located at the lower boundary, i.e., in the most distant area from the EMG electrodes.

Next, we evaluate the quality of the innervation pulse trains that were recovered by the gCKC algorithm in our scenarios. We compare the stimulation times calculated by DEMUSE with the stimulation times of the simulation. [Figure 1.21a](#) shows an excerpt of the detected pulse trains of the second scenario with 20 MUs in [Fig. 1.20](#), where the gCKC algorithm recovered 13 MUs. We observe for some MUs that the recovered stimulation times are consistently shifted in time. This effect is especially visible for MUs 16 and 18.

The reference times given by the black markers in [Fig. 1.21a](#) correspond to the times when the fibers were stimulated in the simulation in OpenDiHu. The detected MU ac-

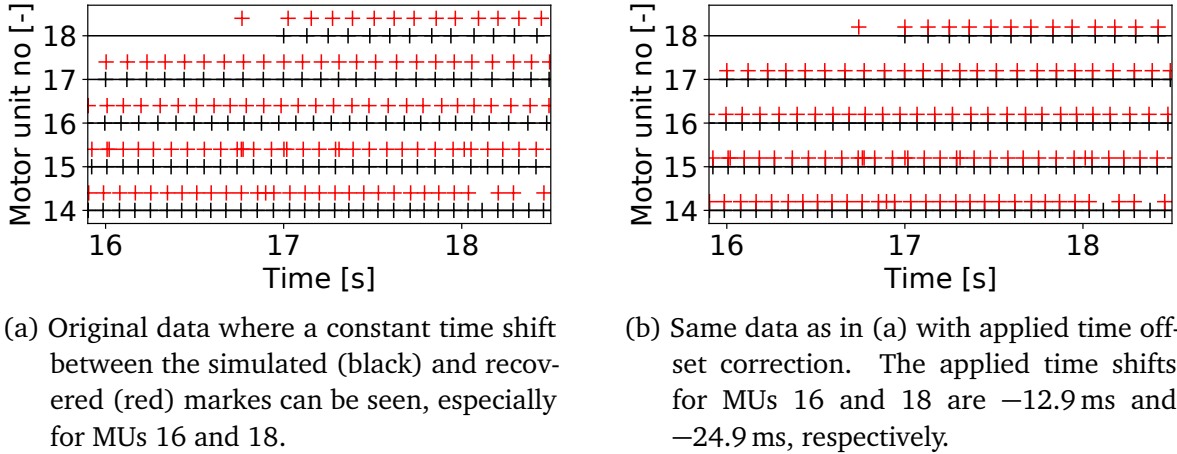


Figure 1.21: Excerpts of the detected firing times of MUs 14 to 18 in the second scenario with 20MUs. The stimulation times of the simulation are given by black markers, the recovered times are visualized by red crosses.

tivations in DEMUSE, however, correspond to the times when the MU action potential shapes in the EMG recording reached their maximum. Moreover, the exact times when particular MUs reach particular EMG electrodes depend on the distance of the electrodes to the innervation points of the MUs. The further the electrodes are away from the neuromuscular junctions along the muscle, the higher is the delay of the recorded spikes to the corresponding innervation pulses. Thus, the constant time shifts in the pulses detected by the gCKC algorithm are valid and have to be accounted for in the evaluation of the decomposition performance.

We correct for these time shifts by adding constant time offsets Δt_k to the recovered innervation pulse trains. For every MU k , the algorithm finds the matching pairs of simulated and recovered pulses and optimizes the value of Δt_k such that the time differences in these pairs after shift correction get minimal.

[Figure 1.21b](#) shows the same extract of MU activity as in [Fig. 1.21a](#) with applied time offsets. The time offsets for MUs 14 to 18 in this example are given as

$$\begin{aligned} \Delta t_{14} &= -2.4\text{ ms}, & \Delta t_{15} &= -1.1\text{ ms}, & \Delta t_{16} &= -12.9\text{ ms}, \\ \Delta t_{17} &= -2.9\text{ ms}, \quad \text{and} & \Delta t_{18} &= -24.9\text{ ms}. \end{aligned}$$

[Figure 1.21b](#) shows that the recovered pulses now match the simulated data very well. The non-matching pulses are clearly false positive detections.

To compare the recovered MU times between the scenarios, we evaluate metrics such as the rate of agreement. The MU firing times in the simulation serve as the ground truth to

which we compare the recovered MU times. We identify true positive (TP), false positive (FP) and false negative (FN) recovered pulses, depending on whether a matching time to a recovered pulse can or cannot be found in the simulation data within a tolerance of $\varepsilon = 5$ ms. The rate of agreement (RoA) between the gCKC algorithm output and the ground truth data is then computed by

$$\text{RoA} = \frac{\text{TP}}{\text{TP} + \text{FP} + \text{FN}}.$$

In the first scenario with 20 MUs in Fig. 1.17, the RoA for MUs 16, 18 and 19 is above 99.7% and slightly lower at 82.2% for MU 20. Here, only 296 of the 334 detected pulses were true positives, corresponding to a precision of 88.6%.

In the second scenario with 20 MUS presented in Fig. 1.20, all valid MUs except one have RoA values of above 94.5 %. Five MUs are even detected perfectly with 100 % rate of agreement. MU 9 is the only detected MU with a degraded RoA of approximately 57.9 %. However, the RoA improves to 98.1 %, if the tolerance ε for matching pulses is relaxed to 10 ms. This shows that the RoA metric also depends on a proper value for the tolerance ε , and that some of the innervation pulse trains detected by DEMUSE can have varying accuracy in a range of less than 10 ms.

While the gCKC algorithm can be used for EMG decomposition of previously recorded signals in a controlled environment, it is less suited for real-time applications such as human-machine interfaces (HMI). The separation vectors that decompose the electrode signals and infer the MU innervation pulse trains can be computed in a training phase. However, their application on new data requires a certain history of previously captured signals to calculate the decomposed MU pulses. In consequence, the predictions are delayed, which is usually undesirable in HMI applications. Furthermore, the system is sensitive to noisy data.

A fundamentally different approach to EMG decomposition is the use of sequence-to-sequence learning methods provided by recurrent neural networks. The authors of [Cla21] used a gated recurrent unit (GRU) network for this task. The network was trained using the output of the gCKC algorithm and was subsequently able to decompose surface EMG signals into innervation pulse trains. The approach was shown to be robust and to outperform gCKC for low signal-to-noise ratios.

To assess, whether our simulations of surface EMG can be used for the supervised learning of GRU networks for EMG decomposition, we tried in a first step to reproduce the studies of [Cla21], where the GRU is trained with the output of the gCKC algorithm.

Additionally, we trained a GRU network directly on the simulated EMG data. These tasks were carried out in the masters project of Srijay Kolvekar and were supervised by Lena Lehmann and me. For details on the methods and results, we refer to the literature [Cla21] and the project report [Kol21].

In this project, the EMG decomposition of a GRU network trained with raw innervation pulse trains obtained from the gCKC algorithm, similar to the literature, showed a large number of false positive and false negative predictions. However, a different setup using MU labels instead of raw pulse trains showed promising results. Every discrete point in time (according to the EMG sampling frequency) was either associated with the class of the currently active MU or with the background class, when no MU was activated at the time. This classification problem had a large class imbalance, as the background class was active for 86 % of the timesteps. The issue was mitigated by using class weights. The GRU network was trained with simulation data and yielded per-class rates of agreement of up to 72 % for the two scenarios with 20 MUs shown in Figures 1.17 and 1.20.

Figure 1.22 presents an excerpt of the resulting predictions of a GRU network that was trained with simulation results. We used the simulation of the second scenario with 20 MUs, which is shown in Fig. 1.20. The black markers in Fig. 1.22 indicate the stimulation times used in the simulation. The red markers correspond to the recovered times by the gCKC algorithm. Out of the shown MUs, only MUS 9 and 10 were recovered by the gCKC algorithm. The blue markers denote the GRU predictions. Correction of time offsets was performed for both the gCKC and GRU outputs.

Figure 1.22 shows the best agreement between the two prediction methods for MU 10 with a RoA of 99.6 % for the gCKC algorithm and 72.2 % for the GRU network. In contrast to the gCKC algorithm, the GRU network predicts firings for all MUs. However, the quality is only acceptable for MUs that could also be detected by the gCKC algorithm. For MUs 11 and 12, the RoA for the GRU network is around 30 %.

In future work, the decomposition performance of the GRU networks could be improved by using different training data. For example, the ramp activation in the training data could be replaced by constant tetanic stimulations or training data where different single MUs are activated at a time could be investigated.

In conclusion, the gCKC algorithm is able to decompose artificially generated surface EMG signals. This means that our simulation can be used to evaluate the performance of EMG decomposition algorithms.

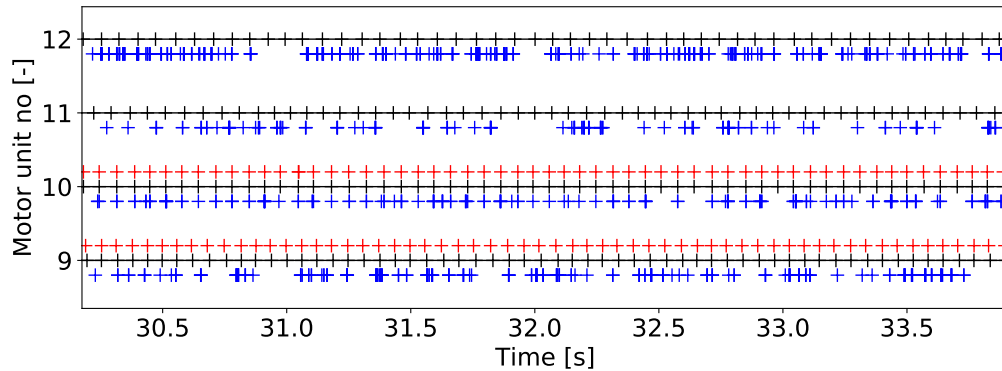


Figure 1.22: Comparison of innervation pulse train predictions of the gCKC algorithm (red), a GRU network (blue) and the ground truth data (black).

The number of detected MUs depends on the relation between MU sizes and on the distance of the MU territories to the electrodes. If the variance of the sizes of the activate MUs is small, such as in Fig. 1.19a, also MU are detected that are far away from the electrodes. If, in the opposite case, the sizes of active MUs are distributed over a large range such as in Fig. 1.18a, only the largest MUs are detectable.

In addition, the amount of adipose tissue between the electrodes and the muscle influences the number of MUs that can be recovered. In our studies, the performance of EMG decomposition was lower for all scenarios with thicker fat layer than for the scenario with a thin fat layer.

The rate of agreement of the determined pulse trains of the DEMUSE software was above 95 % in most of the cases. Correspondingly, the rate of false positives was low. A time shift between the recovered times and the ground truth data was observed for some pulse trains, however, it can be explained with the delay from first activation to the onset of the EMG signal. As a result, the time shift was corrected for the rate of agreement measurement.

A proof-of-concept implementation of GRU networks showed promising performance for predicting MU firing times from artifical EMG recordings. In future work, the algorithm has to be refined to be comparative to the gCKC algorithm.

1.11 Application: Static bidomain

1.12 Application: Multidomain

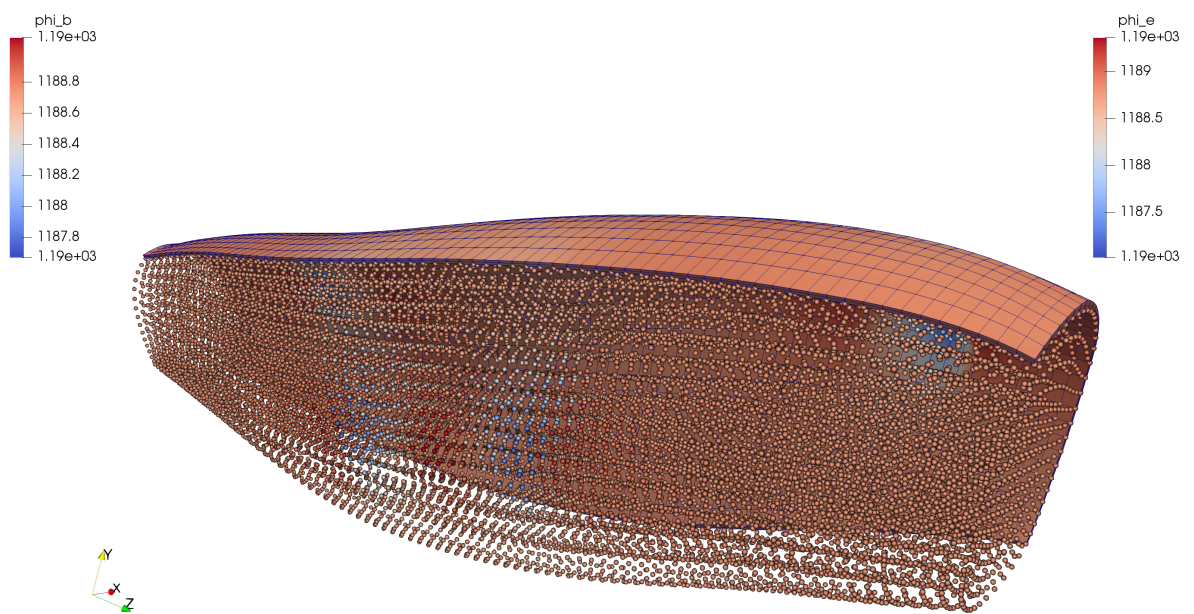
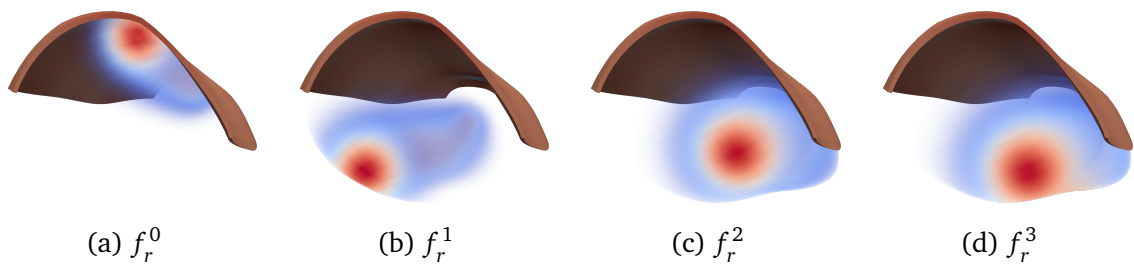


Figure 1.24: multidomain mesh

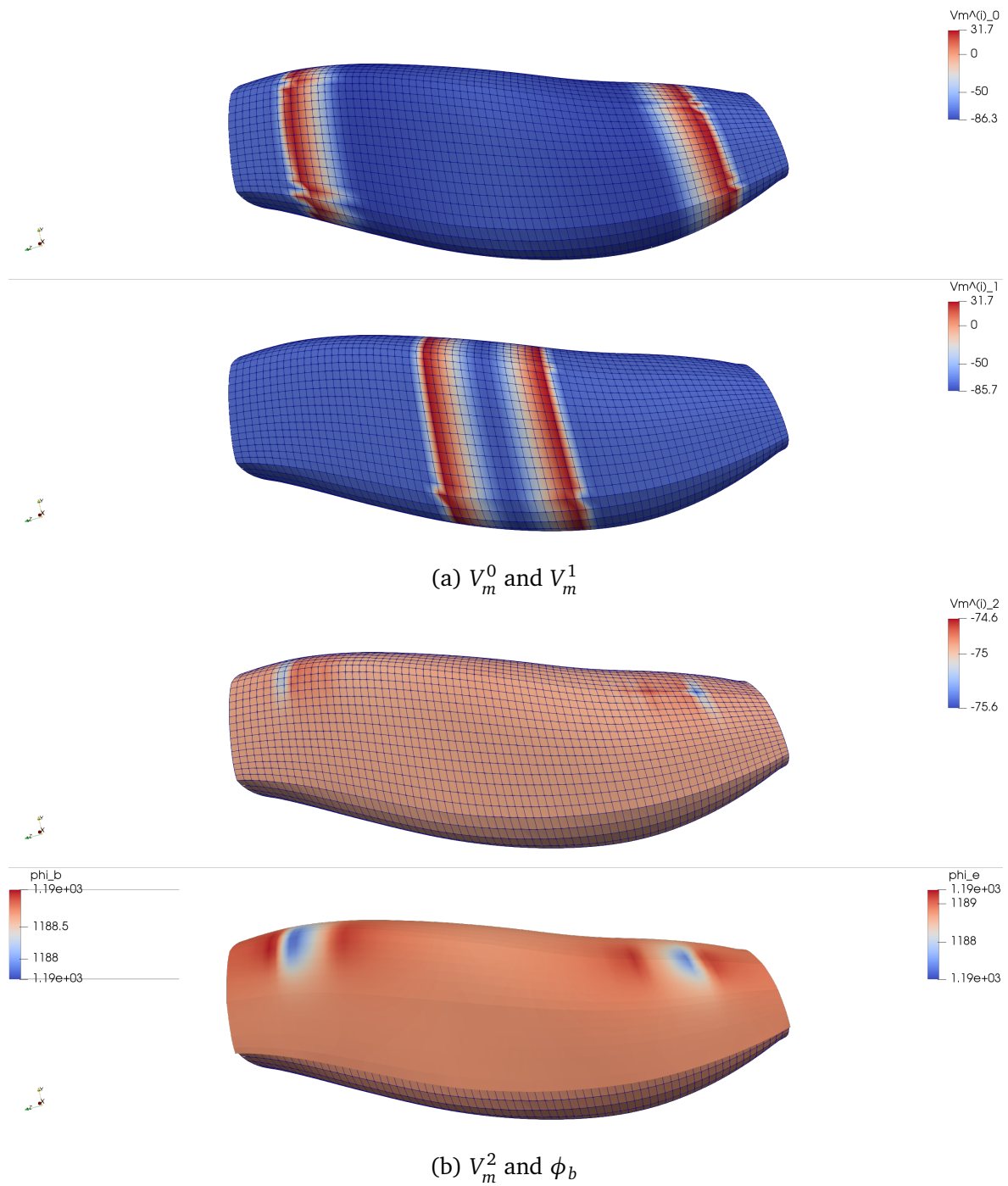


Figure 1.25: gpu.

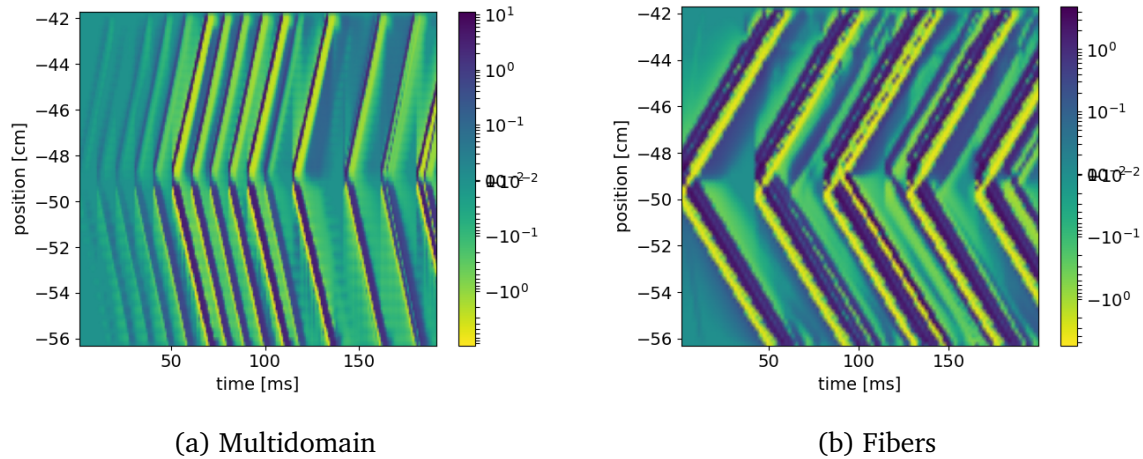


Figure 1.26: Fibers and Multidomain

1.13 Application: Linear mechanics with artifical electrophysiology

1.14 Application: Fibers and Muscle contraction, no-precice

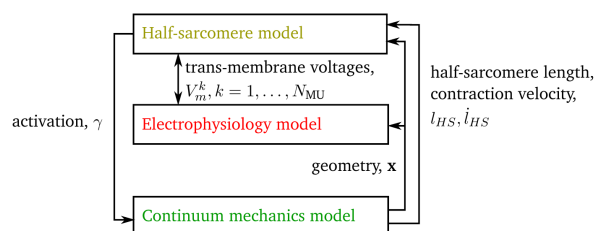


Figure 1.27: prestretch

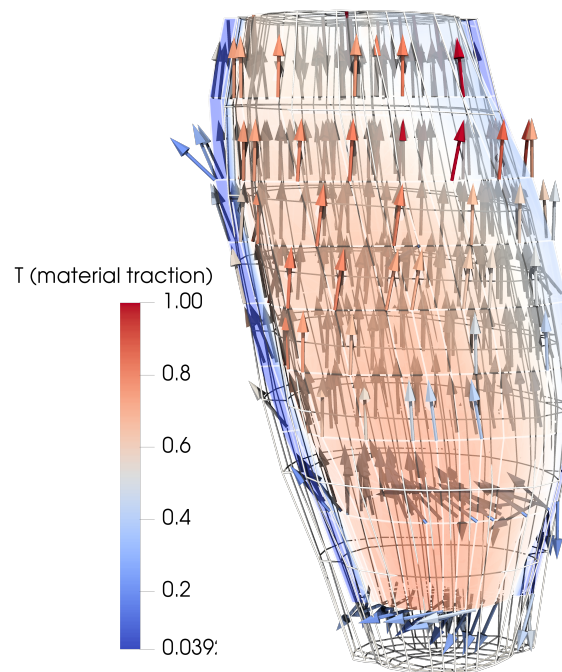


Figure 1.28: solver structure

1.15 Application: Fibers and Muscle contraction, with tendons precise

1.16 Application: Neuromuscular system with Spindles and Prestretch



Figure 1.29: prestretch

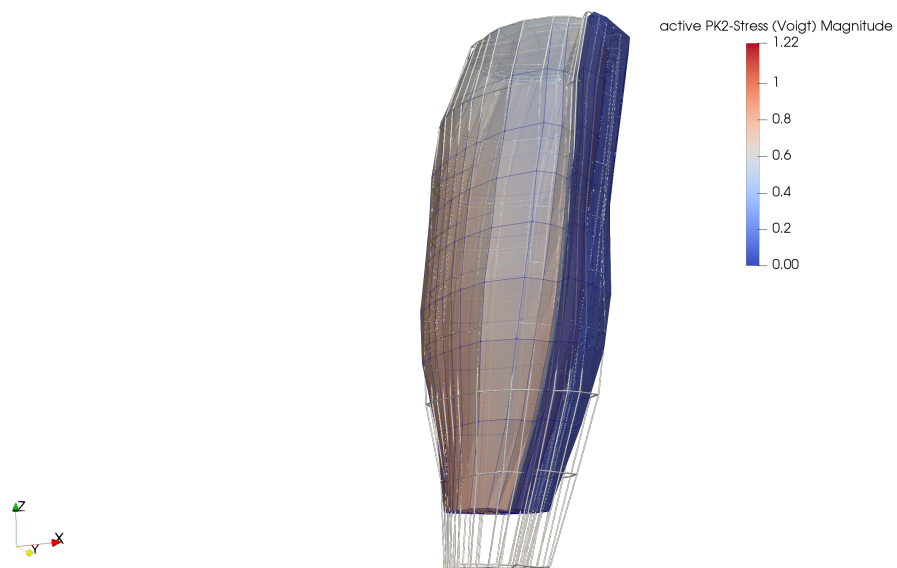


Figure 1.30: Reference and current configuration.

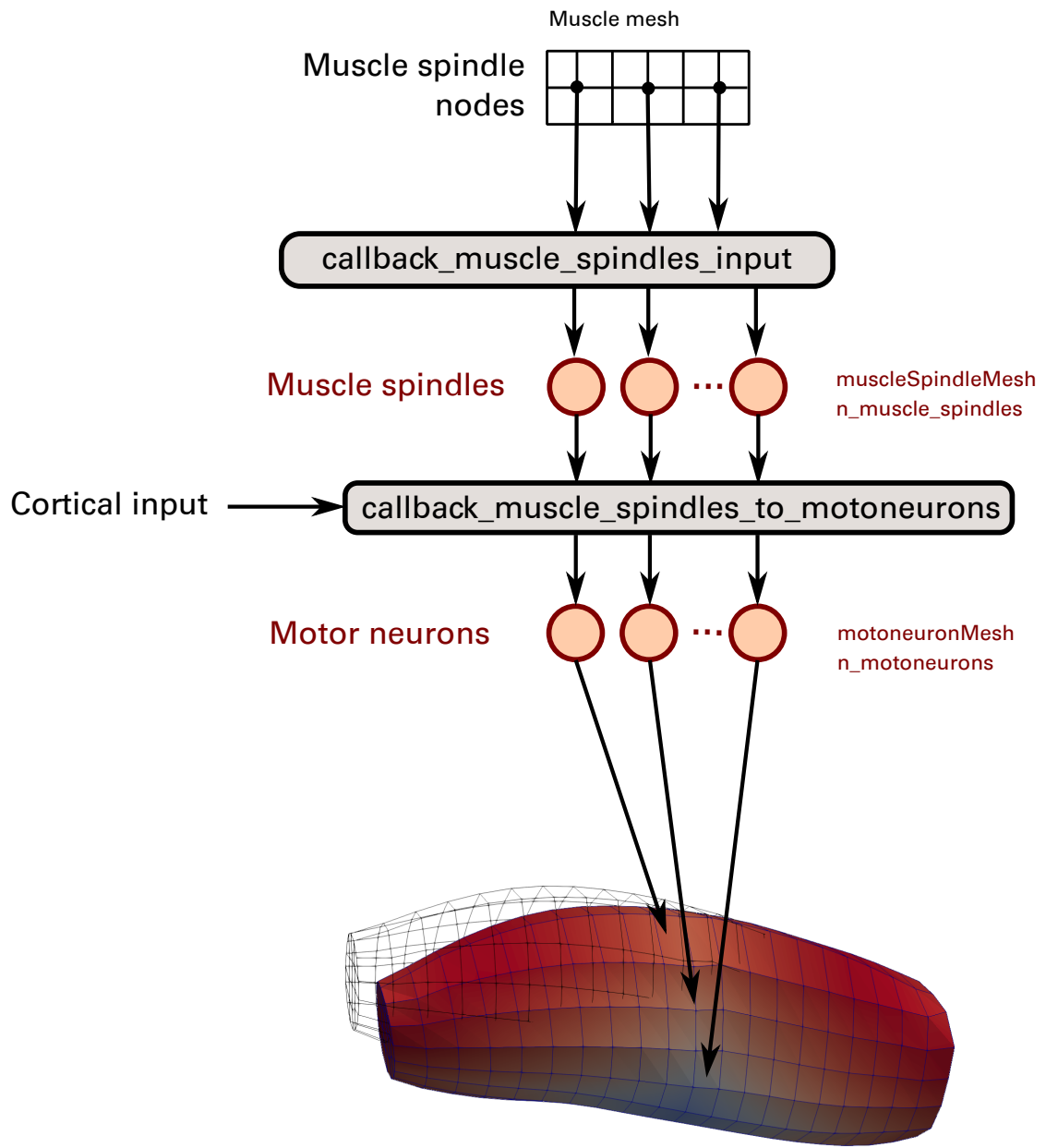


Figure 1.31: Data flow of simulation with spindles and motor neurons

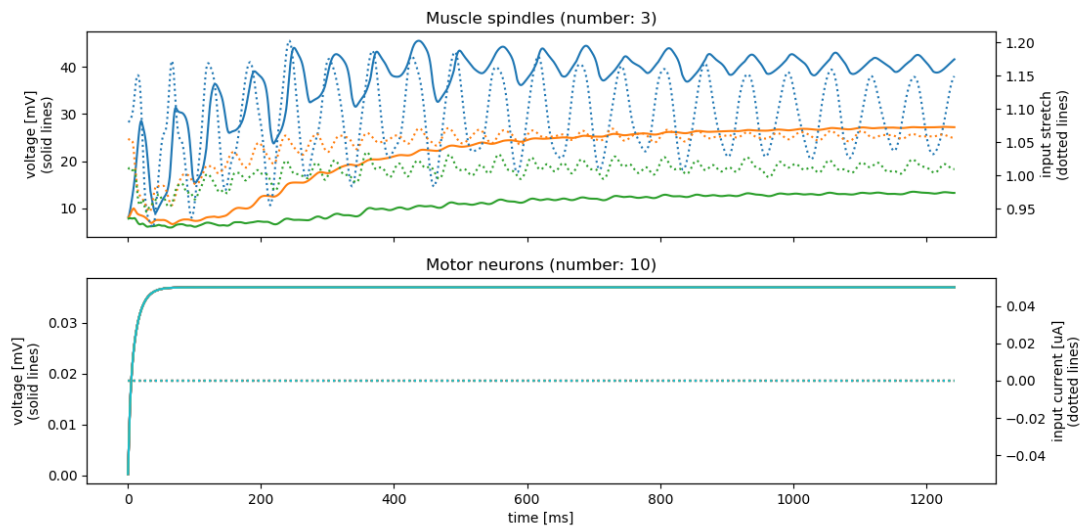


Figure 1.32: Activation data of sensors and neurons

1.17 Application: Neuromuscular system with More Sensor Organs

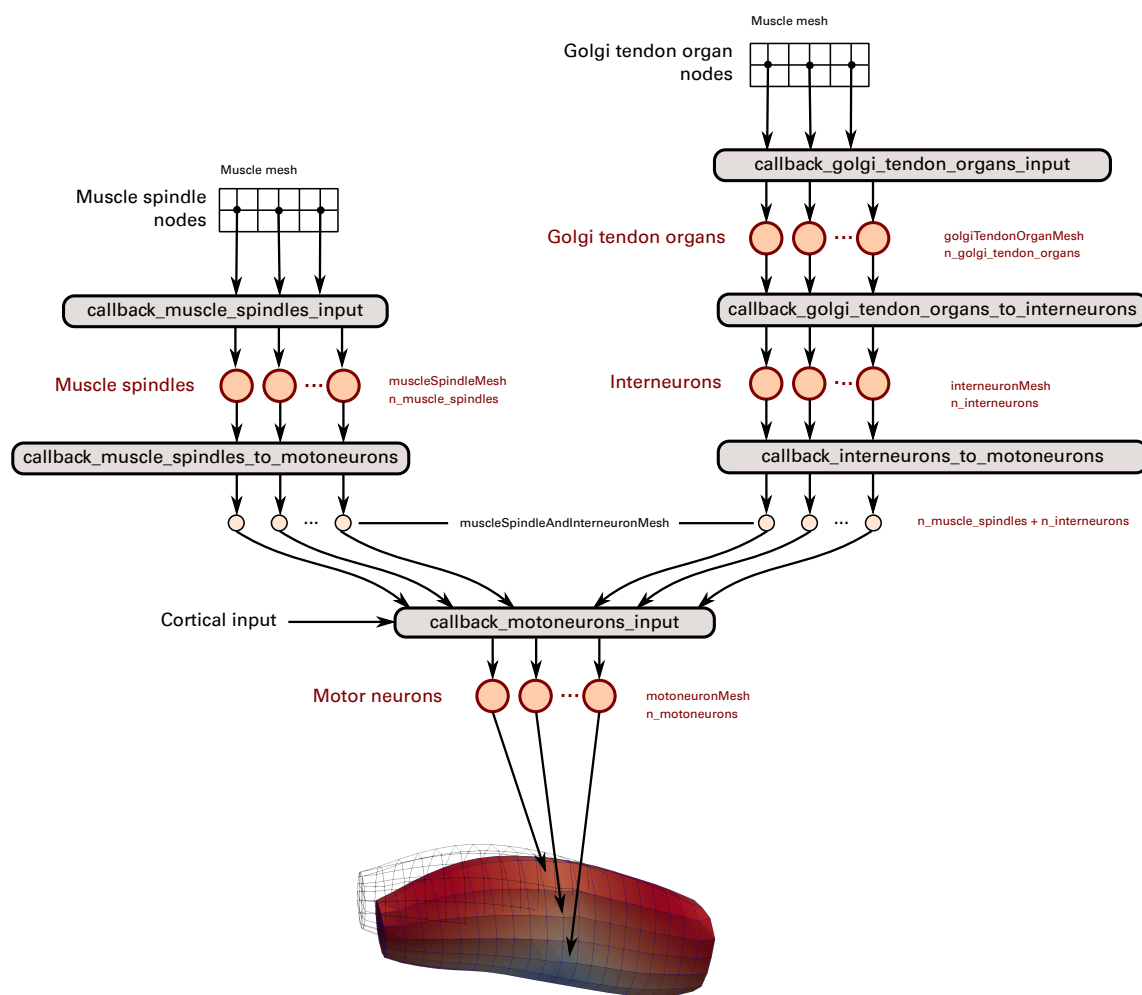


Figure 1.33: Data flow of simulation with spindles, Golgi tendon organs and motor neurons

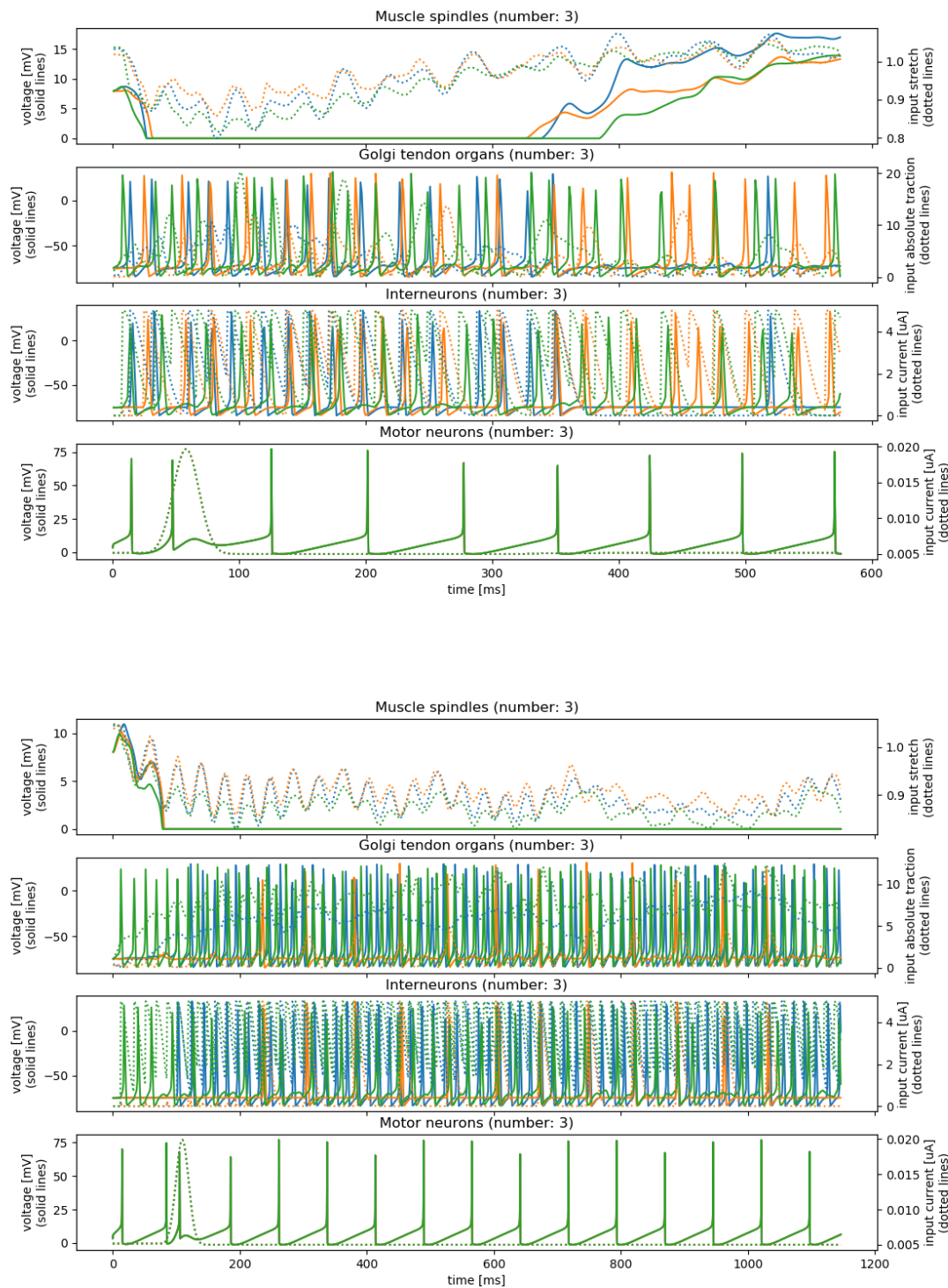


Figure 1.34: Activation data of sensors and neurons

Bibliography

- [Cla21] **Clarke**, A. K. et al.: *Deep learning for robust decomposition of high-density surface emg signals*, IEEE Transactions on Biomedical Engineering 68.2, 2021, pp. 526–534, [doi:10.1109/TBME.2020.3006508](https://doi.org/10.1109/TBME.2020.3006508)
- [Fei55] **Feinstein**, B. et al.: *Morphologic studies of motor units in normal human muscles*, Cells Tissues Organs 23.2, 1955, pp. 127–142
- [Hol07a] **Holobar**, A.; **Zazula**, D.: *Multichannel blind source separation using convolution kernel compensation*, IEEE Transactions on Signal Processing 55.9, 2007, pp. 4487–4496, [doi:10.1109/TSP.2007.896108](https://doi.org/10.1109/TSP.2007.896108)
- [Hol07b] **Holobar**, A.; **Zazula**, D.: *Gradient convolution kernel compensation applied to surface electromyograms*, Independent Component Analysis and Signal Separation, ed. by **Davies**, M. E. et al., Berlin, Heidelberg: Springer Berlin Heidelberg, 2007, pp. 617–624, isbn:978-3-540-74494-8
- [Hol08] **Holobar**, A.; **Zazula**, D.; **Merletti**, R.: *Demusetool-a tool for decomposition of multi-channel surface electromyograms*, 2008
- [Klo20] **Klotz**, T. et al.: *Modelling the electrical activity of skeletal muscle tissue using a multi-domain approach*, Biomechanics and Modeling in Mechanobiology 19.1, 2020, pp. 335–349, ISSN: 1617-7940, [doi:10.1007/s10237-019-01214-5](https://doi.org/10.1007/s10237-019-01214-5), <https://doi.org/10.1007/s10237-019-01214-5>
- [Kol21] **Kolvekar**, S.: *Gated Recurrent Unit Network for Decomposition of Synthetic High-Density Surface Electromyography Signals*, MA thesis, Pfaffenwaldring 47, 70569 Stuttgart, Germany: Institute for Signal Processing and System Theory, University of Stuttgart, 2021
- [Mac06] **MacIntosh** B., R.; **Gardiner** P, F; **McComas** A., J.: *Skeletal Muscle: Form and Function*, Second, Human Kinetics, 2006
- [Mac84] **MacDougall**, J. D. et al.: *Muscle fiber number in biceps brachii in bodybuilders and control subjects*, Journal of Applied Physiology 57.5, 1984, PMID: 6520032, pp. 1399–1403, [doi:10.1152/jappl.1984.57.5.1399](https://doi.org/10.1152/jappl.1984.57.5.1399), eprint: <https://doi.org/10.1152/jappl.1984.57.5.1399>, <https://doi.org/10.1152/jappl.1984.57.5.1399>